Design and Characterization of a Fluidic FET for Flow Control in Micro and Nanochannels

Francesco Bonotto

September 30, 2010

Abstract

In this thesis we characterize the behavior of FFET(*Fluidic Field Effect Transistor*) for flow control in micro and nanochannels. An equivalent electrical model is developed for calculating the change of ζ potential when a voltage difference is applied between the channel walls and the bulk fluid. In particular, we generalize different models to consider the effect of electrolyte concentration and pH, oxide thickness and temperature on the ζ potential versus the gate voltage applied on the control electrode. Furthermore, a numerical model for the fluid flow in the channel will be analyzed to study the effect of a step change in zeta potential. We will show the fabrication process of microchannel devices, focusing on the microchannel preparation and the metal/oxide deposition on glass slides. We run current monitoring experiments in order to observe the effects of the gate voltage on the fluid flow. Finally we fit the experimental data with the theoretical models.

Sommario

L'obiettivo di questa tesi è caratterizzare il comportamento di Fluidic FET (*Fluidic Field Effect Transitor*) per il controllo del flusso in micro e nano canali. Un equivalente modello elettrico è stato sviluppato per calcolare la variazione nel potenziale di parete (potenziale ζ) quando una differenza di potenziale è applicata tra le pareti del canale e il fluido. In particolare sono stati generalizzati diversi modelli presenti in letteratura con lo scopo di considerare l'effetto della concentrazione e del pH dell'elettrolita, dello spessore dell'ossido e della temperatura nella relazione tra il potenziale ζ e la tensione applicata all'elettrodo di gate. Un modello numerico del movimento del fluido all'interno del microcanale verrà utilizzato per lo studiare l'effetto della presenza di una variazione a gradino del potenziale ζ. Verrà inoltre illustrato il processo di fabbricazione di dispositivi FFET, focalizzandosi sia sulla preparazione dei microcanali sia sulla deposizione del metallo e dell'ossido su lastrine di vetro. Verrano presentati i risultati degli esperimenti di monitorizzazione della corrente (*current monitoring*) per osservare gli effetti della tensione di gate nel movimento del fluido. Infine verranno comparati i risultati sperimentali e delle simulazioni numeriche.

Preface

The present thesis is submitted as fulfillment of the prerequisites for obtaining the M.Sc. in Electrical Engineering at the University of Padova, Italy (Università degli Studi di Padova). The duration of this 21 ECTS credits project is a 6 months period from April 2010 to September 2010. The work has been carried out at the University of California, Santa Barbara (UCSB) in the Nanolab headed by Dr. Sumita Pennathur and with the supervision of Prof. Gaudenzio Meneghesso, professor of microelectronics at the Department of Electrical Engineering at the University of Padova. I am deeply grateful to her for letting me become a part of the UCSB Nanolab and helping me during my stay here at UCSB. I wish to thank Prof. Meneghesso to give me the opportunity to prepare this thesis abroad, permitting me to apply my engineering knowledges to a research field that is not covered in my home university. I wish to thank everyone in the UCSB Nanolab for helping me during this amazing experience, in particular Alessio Lenzi, Alex Russell, Andrew Crumrine, Francesco Viola, Jared Frey, Jesper Kristensen, Jess Sustarich, Kristian Jensen, Mariateresa Napoli, Mathias Bækbo Andersen, Nolan Pasko, Sumita Pennathur, Tom Wynne, Trent Huang, and the rest of this amazing group. I wish to thank also my new friends that lived this amazing experience with me, specially Fabio Gini, Franco Caporale e Lorenzo Moro. A special thank also to Valerio "Mitch" Michielan and to all the people that walked this five years of university with me. Finally, I really wish to thank my mum Gabriella, my dad Tiziano and my sister Federica, for helping me during all my studies and that had made possible my experience in California.

Contents

Abstract **i**

Sommario **iii**

Preface **v**

1 Introduction **1**

1.1 Microfluidics and Nanofluidics 1

1.2 Field Effect Flow Control 1

1.3 Outline of the thesis 2

2 Theoretical Concepts **5**

2.1 Channel wall surface models 5

2.2 Basic Electrokinetic Theory 6

2.2.1 The Continuity Equation 6

2.2.2 The Electrodynamic Equations 8

2.2.3 The Navier-Stockes Equation 9

2.2.4 The Chemical Potential 9

2.2.5 The Poisson-Boltzmann Equation 10

2.3 Conductance of a Rectangular Channel 11

2.3.1 Electromigration Conductance 13

2.3.2 Advection Conductance 13

2.3.3 Conductance in the Bulk Regime 14

2.4 Chemistry Background 15

2.4.1 Chemistry of Aqueous Solutions 15

2.4.2 Buffer preparation 16

3 Field Effect Flow Control 19

3.1 Field Effect in Microfluidic devices 19

3.2 Three Capacitors Model 22

3.2.1 Temperature Dependence 26

3.3 Distributed Model 27

3.4 Simulation 27

4 Fabrication of microfluidic chips 33

4.1 Basic Procedures 34

4.1.1 Standard Cleaning Procedure 34

4.1.2 Lithography 35

4.2 Mold for PDMS Microfluidics Devices 38

4.2.1 Shrinky Dink Mold 39

4.2.2 PR Mold 40

4.2.3 Glass Mold 43

4.2.4 Silicon Mold 45

4.3 Fabrication of gate electrodes on glass 49

4.3.1 Cleaning and photolithography 49

4.3.2 Trench etching 50

4.3.3 Metal evaporation 50

4.3.4 Metal lift-off 52

4.3.5 PECVD oxide deposition 52

4.3.6 Electrodes vias 54

4.3.7 Chemical Mechanical Polishing 54

4.4 Microchannel fabrications 56

4.4.1 Glass microchannel 56

4.4.2 PDMS microchannel 56

4.5 Bonding 58

4.5.1 Glass-PDMS Bonding 58

4.5.2 Glass-Glass Bonding 60

5 Measurement of EOF and FEFC **61**

5.1 $2pK$ model simulation 61

5.2 Fluid Flow in the Microchannel 61

5.3 Current monitoring measurements 63

6 Conclusion and Outlook **69**

Bibliography **71**

List of Figures

2.1 Solid/fluid interface models 7

3.1 MOS transistor 20
3.3 Gouy-Chapman-Stern model 23

4.1 Mask for microchannel fabrication. 33
4.3 Ultrasonic cleaner 34
4.4 HMDS hood 36
4.5 Turnable chuck 36
4.6 Hot plate 37
4.7 Karl Suss MJB3 mask alignment 38
4.8 Dektak profilometer 39
4.9 Shrinky Dink mold 41
4.10 Shrinky Dink Dektak profile 41
4.11 PR mold microscope 42
4.12 PR mold Dektak profile 43
4.13 Dektak profiles of glass molds 44
4.14 BHF etch rate 44
4.15 Furnace for oxide grown 46
4.16 KOH etch rate 48
4.17 Metal evaporator 51
4.18 PECVD machine 53
4.19 CMP setup 55
4.20 CMP machine 55
4.21 Microchannels in glass 56

4.22 Liquid PDMS 58
4.23 Plasma bonder 59
4.24 PDMS-glass devices 59

5.6 Current monitoring setup 66

List of Tables

4.1 Metal deposition 52
4.2 PECVD generators 53
4.3 PECVD machine 53
4.4 PECVD data 54
4.5 Chemical composition of microscope slides (Fisher Brand). 57

Chapter 1

Introduction

1.1 Microfluidics and Nanofluidics

Microfluidics and nanofluidics are typically defined as the science that studies the behavior of fluids in structures with characteristic dimension in the range 0-100μm and 0-100 nm, respectively. The Nanoscale Device Laboratory known as the Nanolab is a part of the Mechanical Engineering Department at University of California, Santa Barbara (UCSB) under the direction of Dr. Sumita Pennathur. The research is focused on novel studies of chemical and biological species within fabricated nanoscale devices. The research goals spanning the fields of Physics, Biology, Chemistry and Engineering.

In the next chapter will be explained the basic electrokinetic theory to provide a general background on micro- and nanofluidics. The most important phenomenon that will be treated throughout this thesis will be the concept of *electroosmosis*. We refer to *electroosmosis* as the motion of a polar liquid under the influence of an applied electric field.

1.2 Field Effect Flow Control

The field of the microfabricated devices has made a remarkable progress toward the miniaturization of complex systems. In particular, one of the most interesting field of application of micro/nano-fluidics devices is the assembly of lab-on-a-chip

(LOC). A LOC is a device that integrates one or several laboratory functions on a single chip. Usually LOC devices are also named as Micro Total Analysis Systems (μTAS). In these devices, where usually complex microchannels networks are present, electroosmosis has an important part as fluid flow control. Electroosmosis can be permanently altered changing the buffer pH, changing the buffer concentration or coating the inner wall of the channels. These techniques change the properties of the system and lead to a new static electroosmotic mobility. Instead, it has been proved that applying a perpendicular electric field across the wall of capillary used in typical electrophoresis systems it is possible to change dynamically the electroosmotic mobility, altering the fluid flow inside the channel [1]. This dynamic control is known as *Field Effect Flow Control*. This field has been intensively studied in the last decade. The goals of this thesis are fabricated microchannels devices with embeded and insulated metal electrodes and create an equivalent electrical model of the fluid/insulator/metal system. Furthermore, a comparison with the Metal Oxide Semiconductor Field Effect Transistor will be provided. Lastly a characterization of the fluid movement in the channel will be presented. The possibility to locally control the fluid flow inside a networks using an external electric field will avoid the use of mechanical valves that requires a huge external apparatus compared to the dimensions of the chip. Instead, the miniaturization and integration of a voltage source with an integrated control system is compatible with the state of the art electronic circuits. The necessity of small and portable source/control system is an ineluctable requirement for a real Lab On a Chip device.

1.3 Outline of the thesis

Chapter 2: Background on Microfluidics Theory

In this chapter we will present an overview on the solid/liquid interface and the governing equations for a nanochannel system. In particular, we will introduce the ζ potential, the concepts of migration and advection currents and review the basic chemistry relations.

Chapter 3: Field Effect Flow Control

In this chapter we will study the field effect phenomena deriving an equivalent electrical model for the system. A Matlab® model will be designed to calculate the dependence of the ζ potential on the gate voltage, considering the effects of concentration, pH and oxide thickness. Furthermore, a Matlab® script that implement a model for the solid/liquid interface will be used to solve the equation for the current inside the channel.

Chapter 4: Fabrication

In this chapter all the microchannel fabrication techniques used in this project will be detailed explained. Advantages and disadvantages will be explored, and moreover all the failures will be analyzed.

Chapter 5: Experimental

In this chapter we will present the results from Matlab® flow/current simulations and compare them with the first experimental results obtained used the devices fabricated during the project.

Chapter 6: Conclusion

In this chapter we draw the conclusion of the the project and present an outlook for future studies on the application of field effect flow control in Lab On a Chip devices.

Chapter 2

Theoretical Concepts

In order to provide a theoretical background for the present thesis, in this chapter we introduce the basic equations and notions useful on the description of nano- and microfluidics systems. Since nanofluidics is an interdisciplinary research area, theoretical concepts and mathematical framework related to the electrokinetic theory, fluid dynamics, surface chemistry and chemistry of the solutions will be presented.

2.1 Channel wall surface models

Through this section we will review the history of the solid/liquid interface models. For an exhaustive treatment of the topics we suggest Ref.[2]. An accurate description of the solid surface in contact with a liquid is very important to correctly develop the electrokinetic theory. The necessity of an accurate interface model increases in micro- and nanofluidic where the dimension of the devices becomes comparable to the critical length of the phenomena that take place near the walls. In 1879, Hermann von Helmholtz proposed a very simple double layer model: it consisted of a charged flat surface and a spatial countercharge with opposite signs as compared to that of the wall, equivalent to a capacitor as shown in Figure 2.1(a). Luois-Georges Gouy in 1910 and, autonomously, David Leonard Chapman in 1913, developed a theory for the double layer, where a diffuse space charge is included as illustrated in Figure 2.1(b). In the Gouy-Chapman model is introduced the Debye length λ_{D}, an important parameter that characterized the

thickness of the diffuse layer. These models did not predict the results of electrokinetic experiments and only in 1924, Stern combined the two models into the Gouy-Chapman-Stern model shown in Figure 2.1(c) that confirmed experimental results. In this model both an immobile monoatomic layer (also known as the Stern layer) modeled as a capacitor and diffuse layer are present. This is so far the most common model used to describe a surface touching an electrolyte. Other models were introduced in the last decades as the three and the four layers models. For a through description of these models we recommend Ref. [3], [4], [5], [6] and [7]. Based on the Gouy-Chapman-Stern model, Kristian Lund Jensen and Jesper Toft Kristensen developed at Nanolab, UC Santa Barbara a new model called 2pK-Model [8], shown in Figure 2.1(d). This model has been implemented in MatLab and it will be used throughout the thesis to simulate the electrokinetic phenomena that will take place in our real devices.

2.2 Basic Electrokinetic Theory

In this section we present the governing equations of fluid mechanics, electrodynamics and statistical physics that will be relevant throughout the thesis. These fundamental equations will be introduced with the assumption that the continuum hypothesis is valid. It states that the fluid properties vary continuously from one point to another, neglecting the fact that the fluid is made up of discrete molecules. The smallest system dimension allowable for a continuum description is $\sim 3nm$ [9], orders of magnitude lower than the critical dimension of our devices. For this reason, the continuum hypothesis is acceptable.

2.2.1 The Continuity Equation

A continuity equation in physics is a differential equation that describes the transport of a conserved quantity. In the case of transport of a fluid, assuming that a given compressible fluid cannot spontaneously generate or lose mass in a lossless channel, the continuity equation expresses mass conservation and can be written as

$$\partial_t \rho(\mathbf{r}, t) = -\nabla \cdot [\rho(\mathbf{r}, t)\mathbf{v}(\mathbf{r}, t)], \tag{2.1}$$

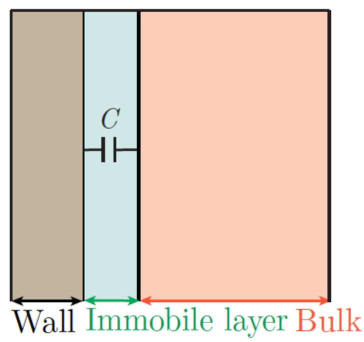

(a) Helmholtz model.

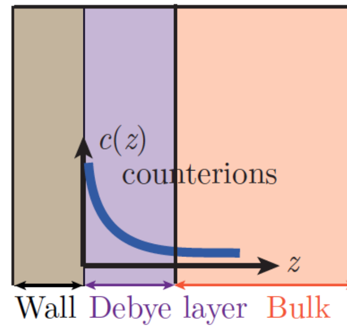

(b) Gouy-Chapman model.

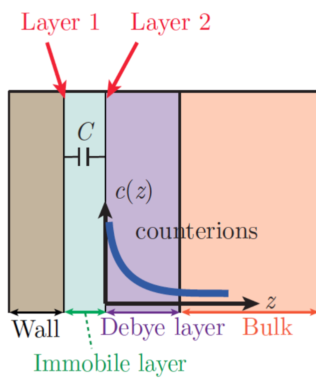

(c) Gouy-Chapman-Stern model.

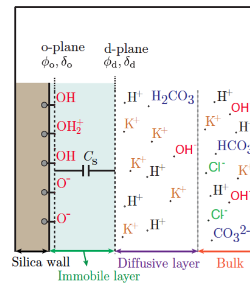

(d) 2pK model.

Figure 2.1: Historical evolution of solid/fluid interface models.

where $\rho(\mathbf{r}, t)$ is the mass density and $\mathbf{v}(\mathbf{r}, t)$ is the velocity vector of the fluid at the spatial point $\mathbf{r}$ at a given time t. Usually, the assumption for an incompressible fluid is that its density does not change both in time and space and thus Equation (2.1) becomes

$$\nabla \cdot \mathbf{v}(\mathbf{r}, t) = 0. \tag{2.2}$$

2.2.2 The Electrodynamic Equations

Throughout this thesis, the hypothesis of a weak and slowly varying currents will be assumed. With this consideration, both the magnetic field strength $\mathbf{H}$ and the magnetic flux density $\mathbf{B}$ can be ignored and the basic electrodynamic equations become

$$\nabla \cdot \mathbf{D} = \rho_{\mathrm{el}}, \tag{2.3a}$$

$$\nabla \times \mathbf{E} = 0, \tag{2.3b}$$

$$\mathbf{D} = \epsilon_0 \mathbf{E} + \mathbf{P} = \epsilon \mathbf{E}, \tag{2.3c}$$

$$\mathbf{J}_{\mathrm{el}} = \sigma_{\mathrm{el}} \mathbf{E}, \tag{2.3d}$$

$$\mathbf{F} = q\mathbf{E} \tag{2.3e}$$

where $\mathbf{D}$, ρ_{el}, $\mathbf{E}$, ϵ_0, $\mathbf{P}$, ϵ, $\mathbf{J}_{\mathrm{el}}$, σ_{el}, $\mathbf{F}$ and q are the electric displacement field, the free spatial charge density, the electric field, the electric permittivity of vacuum, the polarization field, the electric permittivity, the electric current density, the electric conductivity, the electric force and the charge, respectively. In the specific case, the electric field is conservative because its rotation is zero and can be written as the gradient of a function, known in this context as the electric potential function ϕ

$$\mathbf{E} = -\nabla \phi \tag{2.4}$$

For an uniform fluid, the electric permittivity tensor is a constant scalar ϵ. Using Equations (2.3a), (2.3c) and (2.4) we get the Poisson equation

$$\nabla^2 \phi(\mathbf{r}) = -\frac{1}{\epsilon} \rho_{\mathrm{el}}(\mathbf{r}). \tag{2.5}$$

2.2.3 The Navier-Stockes Equation

The Navier-Stokes equation describes the motion of fluid substances. It can be derived from the Newton's second law together with the assumption that both a diffusing viscous and a pressure terms contribute to the fluid stress. For an incompressible fluid under the influence of an electric field, the Navier-Stokes equation reads

$$\rho[\partial_t \mathbf{v} + (\mathbf{v}\cdot\nabla)\mathbf{v}] = -\nabla p + \eta\nabla^2\mathbf{v} + \rho\mathbf{g} + \rho_{\mathrm{el}}\mathbf{E} \tag{2.6}$$

where $\rho\partial_t\mathbf{v}$ is the local acceleration, $\rho(\mathbf{v}\cdot\nabla)\mathbf{v}$ is the advective acceleration, $-\nabla p$ is the pressure gradient force, $\eta\nabla^2\mathbf{v}$ is the viscous force due to shear stress, $\rho\mathbf{g}$ is the gravitational force density and $\rho_{\mathrm{el}}\mathbf{E}$ is the electric force density.

2.2.4 The Chemical Potential

Statistical mechanics describes the differential change in free energy from an incremental addition of an ion in a given low-concentration electrolyte contained in a specific volume of an ideal gas. Assuming that in our problem the free energy is the Gibbs free energy $\mathcal{G}$ the chemical potential μ is defined as

$$\mu \equiv \left(\frac{\partial\mathcal{G}}{\partial\mathcal{N}}\right)_{T,p} \tag{2.7}$$

for a given constant temperature T and pressure p. In order to simplify the problem, it will be assumed that the fluid contains only one electrolyte with opposite valences $\pm N$ with N positive integer. With this assumption, the chemical potential for both negative and positive ionic concentrations at a given spatial point $\mathbf{r}$ can be written as

$$\mu_{\pm}(\mathbf{r}) = \mu_{0,\pm} + k_{\mathrm{B}}T\,\ln\left(\frac{c_{\pm}(\mathbf{r})}{c_0}\right) \pm Ne\phi(\mathbf{r}) \tag{2.8}$$

where $\pm$ refers to positive and negative ions, respectively. c_0 and $\mu_{0,\pm}$ are the concentration and chemical potential without the electrical potential $\phi(\mathbf{r})$. k_{B}, e and $c_{\pm}(\mathbf{r})$ are the Boltzmann constant, the elementary charge and the concentration of the ion at point $\mathbf{r}$, respectively.

2.2.5 The Poisson-Boltzmann Equation

Considering the situation of thermodynamic equilibrium, the chemical potential $\mu_{\pm}$ are constant inside the system. This implies

$$\nabla \mu_{\pm}(\mathbf{r}) = 0. \tag{2.9}$$

Using the equilibrium hypothesis in Equation (2.8), it is possible to derive an equation that related the concentration and electric potential:

$$k_{\mathrm{B}}T\, ln\Big(\frac{c_{\pm}(\mathbf{r})}{c_0}\Big) = \mp Ne\phi(\mathbf{r}) \tag{2.10}$$

In order to solve this equation, the channel wall can be modeled as an infinite planar wall which occupies the half-space $z < 0$. The potential at the wall is called ζ potential and it will be the most important quantity throughout this thesis. In addition, it is assumed that the potential decays to zero at infinity (i.e. far from the wall) $\phi(\infty) = 0$, and the concentration at infinity of negative and positive ion reaches the value $c_{\pm}(\infty) = c_0$. This ensures the overall charge neutrality since the ion valences are equal. These boundary conditions are used to solve Equation (2.10) and obtain the ionic concentration profiles

$$c_{\pm}(\mathbf{r}) = c_0 \exp\Big[\frac{Ne}{k_{\mathrm{B}}T}\phi(\mathbf{r})\Big]. \tag{2.11}$$

Due to equal valences, the total charge density ρ_{el} at any given point $\mathbf{r}$ is

$$\rho_{\mathrm{el}}(\mathbf{r}) = Ne\big[c_{+}(\mathbf{r}) - c_{\text{-}}(\mathbf{v})\big] = -2Nec_0 \sinh\Big[\frac{Ne}{k_{\mathrm{B}}T}\phi(\mathbf{r})\Big]. \tag{2.12}$$

Using this result in Equation (2.5), we derive the so-called Poisson-Boltzmann equation

$$\nabla^2\phi(\mathbf{r}) = 2\frac{Nec_0}{\epsilon} \sinh\Big[\frac{Ne}{k_{\mathrm{B}}T}\phi(\mathbf{r})\Big] \tag{2.13}$$

that can be solved using the assumptions that the potential decays monotonically to zero infinitely far from the wall

$$\phi(\infty) = \partial_z \phi(\infty) = 0 \tag{2.14}$$

The solution of Equation (2.13) using the boundary conditions stated in Equation (2.14) is the so-called Gouy-Chapman solution given by

$$\phi(z) = \frac{4k_\mathrm{B}T}{Ne} \operatorname{arctanh}\Big[\tanh\Big(\frac{Ne\zeta}{4k_\mathrm{B}T}\Big)\exp\Big(-\frac{z}{\lambda_\mathrm{D}}\Big)\Big], \tag{2.15}$$

$$\lambda_\mathrm{D} \equiv \sqrt{\frac{\epsilon k_\mathrm{B}T}{2(Ne)^2 c_0}} \tag{2.16}$$

where λ_D is the Debye length, a characteristic length scale used in nanofluidics. In the Debye-Hünckel limit, the electric potential energy is much smaller than the thermal energy

$$Ne|\zeta| \ll k_\mathrm{B}T, \tag{2.17}$$

and Equation (2.13) can be Taylor expanded to obtain

$$\nabla^2\phi(\mathbf{r}) = 2\frac{(Ne)^2 c_0}{\epsilon k_\mathrm{B}T}\phi(\mathbf{r}) \equiv \frac{1}{(\lambda)^2}\phi(\mathbf{r}). \tag{2.18}$$

The channel can be modeled with two parallel plates with surface at $z = 0$ and $z = h$ and potential ζ. This assumption is equivalent to consider a the channel with an high aspect ratio $h \ll w$ as in the devices that will be tested. The solution to Equation (2.18) with this hypothesis is

$$\phi(\mathbf{r}) = \phi(x, y, z) = \phi(z) = \zeta\frac{\cosh(\frac{z-h/2}{\lambda_\mathrm{D}})}{\cosh(\frac{h}{2\lambda_\mathrm{D}})}, \quad 0 < z < h \tag{2.19}$$

where the electric potential does not depend on the x and y coordinates.

2.3 Conductance of a Rectangular Channel

Referring to the rectangular channel shown of heigh h and width w, in this section we will derive the conductance of the system. With the assumption that the

channel has a high aspect ratio $h \ll w$, the potential due to the charged channel walls can be approximated with an internal potential $\phi_{\text{int}}(z)$, as derived in Equation (2.19). Two metal electrodes are located at each end of the channel inside little tanks so-called reservoirs. When a voltage ΔV is applied between the two electrodes, an external electric field $\mathbf{E}_{\text{ext}}$ is established in the channel direction x:

$$\mathbf{E}_{\text{ext}} = -\nabla \phi_{\text{ext}} = \frac{\Delta V}{L} \mathbf{e_x}. \tag{2.20}$$

The corresponding external potentials are $\phi_{\text{ext}}(x = 0) = \Delta V$ and $\phi_{\text{ext}}(x = L) = 0$, where L is the channel length. Assuming that the external potential does not influence the ion distribution inside the channel and neglecting fringe effects, we can assume a translationally invariant ion disposition in the xy-plane. Therefore, the ζ potential can be considered constant along the channel walls and the charge density is given by

$$\rho_{\text{el}}(z) = -\epsilon \partial_z^2 \phi_{\text{int}}(z). \tag{2.21}$$

The conductance is the degree to which an object conducts electricity, calculated as the ratio of the current that flows to the potential difference present

$$S \equiv \frac{I}{\Delta V} \tag{2.22}$$

The external electric field creates two terms for the electrical current inside the microchannel. The first term is the so-called electromigration current I_{mig}, a current set up by the motion of ions. Due to the charge neutrality of the electrolyte, there are on average the same number of positive (counterions) and negative (co-ions) ions that are moved in opposite direction along the channel, resulting in no net movement of the liquid bulk. Near the walls, in the non-neutral diffusive layer, more counterions are moved toward the negative electrode rather than the co-ions moved toward the positive electrode. Forces between the moving particles and the surrounding liquid accelerates the diffusive layers which start to move relative to the bulk. This mass flow induced by an external electric field is known as electroosmosis. Viscous forces between the fluid in the diffusive layer and the fluid in the bulk accelerates the bulk creating an additional term to the total current called electric advection current I_{adv}. Advection is a transport mechanism of a

substance, or a conserved property, by a fluid, due to the fluid's bulk motion in a particular direction. As a result, the total conductance of the channel is the sum of the migration conductance S_{mig} and the advection conductance S_{adv}

$$S_{\mathrm{tot}} = S_{\mathrm{mig}} + S_{\mathrm{adv}} = \frac{I_{\mathrm{mig}}}{\Delta V} + \frac{I_{\mathrm{adv}}}{\Delta V}. \tag{2.23}$$

2.3.1 Electromigration Conductance

The electromigration current is calculated by integrating the electromigration current density $\mathbf{J}_{\mathrm{mig}}$ given by Equation (2.3d) over the cross area of the channel $\partial\Omega$. With the assumptions that the channel has a rectangular cross section and that electric conductivity σ_{el} is symmetric around the center of the channel at $z = h/2$ due to the symmetry in the internal potential $\phi_{\mathrm{int}}(z)$, the migration current is

$$I_{\mathrm{mig}} = \int_{\partial\Omega} \mathbf{J}_{\mathrm{mig}} \cdot d\mathbf{A} = \int_{-\frac{w}{2}}^{\frac{w}{2}} \int_0^h \sigma_{\mathrm{el}}(z) E_{\mathrm{ext}}\, dxdy = 2\Delta V \frac{w}{L} \int_0^{\frac{h}{2}} \sigma_{\mathrm{el}}(z)\, dz \tag{2.24}$$

and hence the electromigration conductance is

$$S_{\mathrm{mig}} = \frac{I_{\mathrm{mig}}}{\Delta V} = 2\frac{w}{L} \int_0^{\frac{h}{2}} \sigma_{\mathrm{el}}(z)\, dz. \tag{2.25}$$

In Equation (2.24) and Equation (2.25), with the hypothesis of a Boltzmann's distribution profile, the conductivity for $\mathcal{N}$ ions inside the channel is

$$\sigma_{\mathrm{el}}(z) = e \sum_{i=1}^{N} |Z_i| \mu_i c_i(z) = e \sum_{i=1}^{N} |Z_i| \mu_i c_i^{\mathrm{b}} \exp\Big(-\frac{Z_i e}{k_{\mathrm{B}} T} \phi_{\mathrm{int}}(z)\Big), \tag{2.26}$$

where c_i^{b}, μ_i and Z_i are the bulk concentration, the mobility and the valence for the i-th specie.

2.3.2 Advection Conductance

The electroosmotic velocity is the resulting velocity in the channel due to electroosmotic effects. Considering the steady state $\partial_t \mathbf{v}(z) = 0$ in a high aspect ratio $h \ll w$ rectangular cross section channel with an external electric field applied in

the x direction and no-slip condition at the walls $v_x(z=0)=0$ and $v_x(z=h)=0$, the Navier-Stokes equation described in Equation (2.6) can be solved for the velocity profile. With the boundary condition $\phi_{\text{int}}(0)=\phi_{\text{int}}(h)=\zeta$, the electroosmotic velocity becomes

$$\mathbf{v}(z)=v_x(z)\mathbf{e}_x=\left[\phi_{\text{int}}(z)-\zeta\right]\frac{\epsilon}{\eta}\mathbf{E}_{\text{ext}}. \tag{2.27}$$

The electric advection current is given by

$$I_{\text{adv}}=\int_{\Delta\Omega}\mathbf{J}_{\text{adv}}\cdot d\mathbf{A}=\int_{\Delta\Omega}\rho_{\text{el}}(\mathbf{r})\mathbf{v}(\mathbf{r})\cdot d\mathbf{A} \tag{2.28}$$

and when $\lambda_{\text{D}}\ll w$, Equation (3.1) can be used in Equation (2.28) together with Equation (2.26) and obtain

$$I_{\text{adv}}=2\Delta V\frac{w}{L}\frac{e\epsilon}{\eta}\int_0^{\frac{h}{2}}\left[\phi_{\text{int}}(z)-\zeta\right]\sum_{i=1}^{\mathcal{N}}Z_ic_i(z)\,dz,\quad \lambda_D\ll w \tag{2.29}$$

The advection conductance is

$$\begin{aligned}S_{\text{adv}}&=\frac{I_{\text{adv}}}{\Delta V}\\&=2\frac{w}{L}\frac{e\epsilon}{\eta}\int_0^{\frac{h}{2}}\left[\phi_{\text{int}}(z)-\zeta\right]\sum_{i=1}^{\mathcal{N}}Z_ic_i^{\text{b}}(z)\exp\Big(-\frac{Z_ie}{k_{\text{B}}T}\phi_{\text{int}}(z)\Big)\,dz,\quad \lambda_D\ll w\end{aligned} \tag{2.30}$$

In conclusion, the total conductance S_{adv} Equation (2.23) is the sum of electromigration conductance Equation (2.25) and advection conductance Equation (2.30).

2.3.3 Conductance in the Bulk Regime

Conductances in Equation (2.25) and Equation (2.30) depend on the electrolyte concentration. For a high concentration, i.e. $c>10mM$, $\lambda_{\text{D}}\ll h$ and the bulk dominates the channel. In that case the internal potential $\phi_{\text{int}}(z)$ is approximately zero in the channel and the electromigration conductance becomes

$$S_{\text{mig}}\approx\frac{wh}{L}e\sum_{i=1}^{\mathcal{N}}|Z_i|\mu_ic_i^{\text{b}} \tag{2.31}$$

Instead, since the bulk ρ_{el} is zero due to charge neutrality, the advection conductance for a high concentration solution is negligible,

$$S_{\text{adv}} \approx 0 \tag{2.32}$$

For that reason, the total conductance in the bulk regime is given by

$$S_{\text{tot}} = S_{\text{mig}} + S_{\text{adv}} = \frac{wh}{L} e \sum_{i=1}^{\mathcal{N}} |Z_i| \mu_i c_i^{\text{b}} \equiv S_{\text{bulk}}. \tag{2.33}$$

2.4 Chemistry Background

In this section we will explain the fundamental notions of chemistry useful in the field of nanofluidics. For a complete review of the basic principles of electrolyte chemistry for microfluidic electrokinetics we suggest [10] and [11]. Electrolyte is any substance containing free ions that make the substance electrically conductive. A simple example of electrolyte solution is the table salt NaCl dissolved in water, where free ions are created according to the dissociation reaction

$$\text{NaCl}_{(\text{s})} \rightarrow \text{Na}^+_{(\text{aq})} + \text{Cl}^-_{(\text{aq})} \tag{2.34}$$

Buffer solutions are a specific class of ionic solution. A buffer solution is an aqueous solution consisting on a compound of a weak acid and its conjugate base or a weak base and its conjugate acid. The most important property is that the pH of the solution varies very little when a small amount of strong acid or base is added to it. Buffer solutions are used to maintain pH close to a constant value in a spread variety of chemical applications.

2.4.1 Chemistry of Aqueous Solutions

As stated early, a solute in an aqueous solution can divide reversibly into smaller constituents with the dissociation constant measuring the tendency of the con-

stituents to the compound. Consider the dissociation of the solute A_xB_y

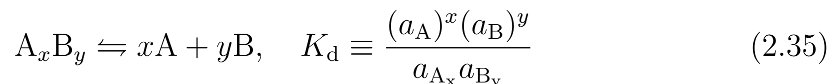

$$A_xB_y \leftrightharpoons xA + yB, \quad K_d \equiv \frac{(a_A)^x(a_B)^y}{a_{A_x}a_{B_y}} \tag{2.35}$$

where a_i is the activity of the ith particle and K_d is the dissociation constant for the reaction. Usually, for an acid-base reaction, the dissociation constant is indicated with K_a and it is normally represented in logarithmic scale

$$pK_a \equiv -\log_{10}(K_a) \tag{2.36}$$

In aqueous solution, pH and pOH are a measure of the acidity and basicity, respectively, with

$$pH \equiv -\log_{10}(a_H) \quad \text{and} \quad pOH \equiv -\log_{10}(a_{OH}) \tag{2.37}$$

where a_H and a_{OH} are the activity of hydronium ions H_3O^+ and hydroxide ions OH^-, respectively. The modern version of pH and pOH is derived considering concentrations instead of activities, obtaining

$$pH \equiv -\log_{10}(c_H) \quad \text{and} \quad pOH \equiv -\log_{10}(c_{OH}) \tag{2.38}$$

2.4.2 Buffer preparation

We now explain the procedure to obtain a specific buffer through an example. The buffer used in the experimental part of the thesis is the Sodium Acetate Buffer. Each specific buffer has a pH range where it works properly as a buffer. In the case of Na Acetate buffer the pH range is 3.7-5.6. The acetic acid weight m_{AA} in gram to obtain a specific concentration c in mol/L for a given final volume V in L is

$$m_{AA} = MW_{AA} \cdot c \cdot V \tag{2.39}$$

where MW_{AA} is the molar weight of the acetic acid [mol/g]. The sodium acetate trihydrate weight m_{SA} to obtain the conjugate base with a specific concentration

c_{SA} for a given final volume V_{SA} is

$$m_{\mathrm{SA}} = MW_{\mathrm{SA}} \cdot c_{\mathrm{SA}} \cdot V_{\mathrm{SA}} \tag{2.40}$$

where MW_{SA} is the molar weight of the sodium acetate. The buffer preparation receipt is:

1. dissolve m_{AA} of acetic acid in $V/2$ of filter deionized (FDI) water;
2. dissolve m_{SA} of sodium acetate trihydrate in V_{SA} FDI water, obtaining the so-called conjugate base;
3. add some conjugate base to the acid solution until the desired pH is reached;
4. add FDI water to new solution to reach the final volume V.

Using different acid and base combination is possible to obtain buffers in different pH range.

Chapter 3

Field Effect Flow Control

The Field Effect is usually referred to the Field Effect Transistor (FET), in particular to the MOSFET (Metal Oxide Semiconductor FET), the basic device present in every nowadays electronic circuits. Referring to Figure 3.1(a), in a MOSFET the current flowing between the Drain and Source terminals is controlled by the voltage applied to a third electrode called Gate. A silicon dioxide layer insulated the metal of the gate from the doped semiconductor present in the bulk. The system Metal-Oxide-Semiconductor can be modeled with a capacitor as shown in Figure 3.1(b) and for this reason the voltage applied to the gate change the charge present at the oxide/semiconductor interface, changing the conductivity of the path between Drain and Source, changing the current. In digital electronics the MOSFET is used as a switch to enable or avoid the passage of current, instead in analog electronic is used as an amplifier. In this chapter we will explain how the Field Effect can be use also in microfluidics science to obtain a flow control without using pressure systems.

3.1 Field Effect in Microfluidic devices

Referring to Figure 3.2, electroosmosis is established applying a voltage difference across the two electrodes inserted in the two reservoirs. Using the nomenclature of the electronic MOSFET, the electrode with higher potential is called *drain* and the other *source*. The current in a micro- nanochannel is originated by two terms,

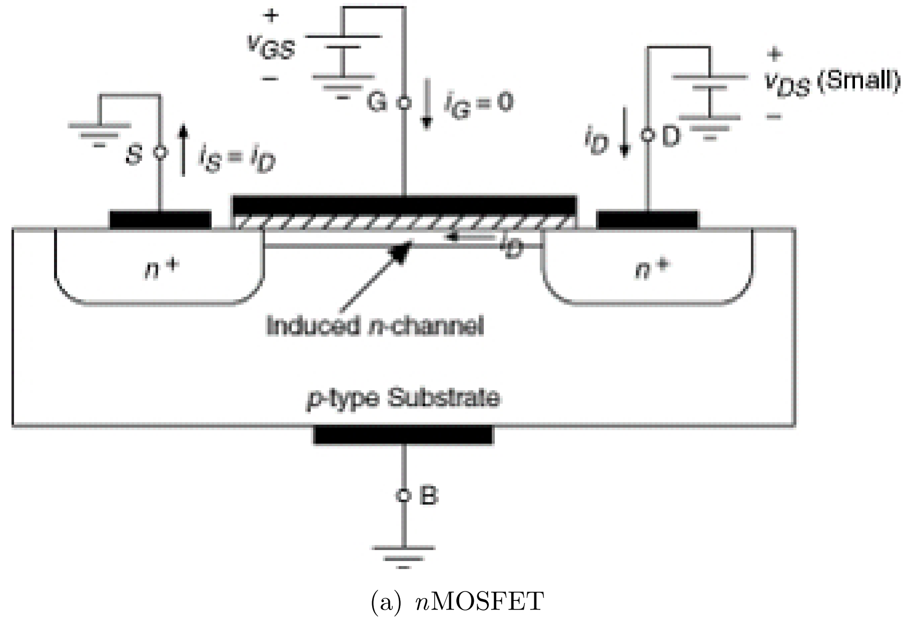

(a) nMOSFET

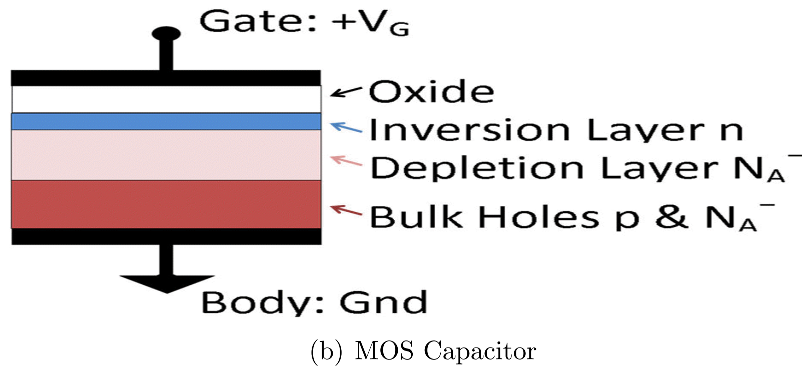

(b) MOS Capacitor

Figure 3.1: The *MOS* transistor.

the migration current and the advection current, derived in Equations (2.24) and (2.29). The last one is related to the movement of the fluid in the channel, and the *electroosmotic velocity* is governed by the Smoluchowski's equation

$$v_{\mathrm{EOF}} = \mu_{\mathrm{EOF}} E_{\mathrm{ext}} = \mu_{\mathrm{EOF}} \frac{V_{\mathrm{D}} - V_{\mathrm{S}}}{L} \tag{3.1}$$

where μ_{EOF} is the so-called *electroosmotic mobility*

$$\mu_{\text{EOF}} = \frac{\epsilon_0 \epsilon_{\text{b}}}{\eta} \zeta \tag{3.2}$$

In Equation (3.2), ϵ_0, ϵ_{b}, η and ζ are the vacuum permittivity, the buffer relative permittivity, the buffer viscosity and the zeta potential. The velocity depends on the proprieties of the fluid and on the zeta potential. Most of the fluids using in micro- and nanofluidics are buffers or electrolytes which permittivity and viscosity are those of water. For this reason, the electroosmotic velocity can be change varying the electric field applied (*i.e.* $V_{\text{D}} - V_{\text{S}}$) or modifying the zeta potential. The first action altered the migration current and also, in the case of a lab-on-a-chip device, usually not only straight channels but also several interconnections are present. The goal for a real flow control is to change the velocity locally in some portion of the circuit and regulating the zeta potential can satisfied this requirement. As illustrated in Figure 3.3, the usually representation for the interface between channel wall and the electrolyte is the *Gouy-Chapman-Stern model*, also named the *double layer model*. When the buffer fills the channel, the walls become charged. Some ions are attracted by these charged sites and are adsorbed creating an immobile layer called Stern layer (or compact layer). Other ions are attracted but not adsorbed and they create the so-called diffuse layer. The profiles of concentration and potential inside this last layer are derived using Equation (2.11) and Equation (2.19). For definition, the zeta potential is the potential at the

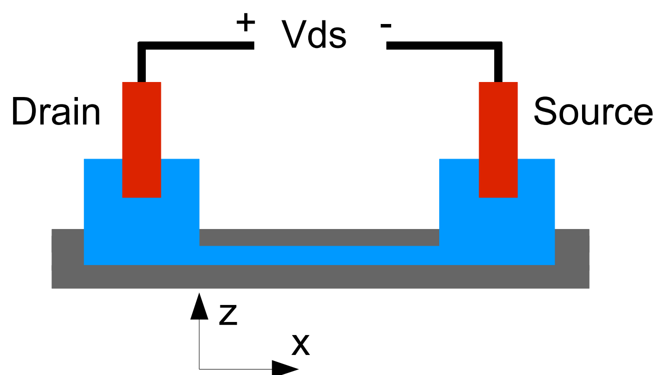

Figure 3.2: Microchannel device for electroosmosis study.

shear plane between mobile/immobile layers. Zeta potential depends on different factors:

- buffer concentration;
- buffer pH;
- channel material;
- temperature.

All these factors lead to a permanent change in zeta potential instead we are looking for a dynamic adjusting. That can be obtained using the Field Effect utilized on the MOS transistor to realize the so-called *Fluid Field Effect Transistor* (FFET). As shown in Figure 3.4, this special transistor consists of a microchannel with two reservoirs with electrodes (called drain and source) and a third electrode covering a channel wall but separated by a insulator layer from the fluid. This electrode is called gate and the electrolyte acts as the induced channel that forms in doped semiconductor bulk of the MOSFET when an appropriate voltage is applied to the control terminal.

In the following sections, an electrical model for the FFET will be presented to relate the change in zeta potential to the gate voltage.

3.2 Three Capacitors Model

The natural model to schematize the FFET system is the three capacitors model shown in Figure 3.5. In that model, each layer is represented as a capacitor. In particular, the system metal-oxide-channel wall is modeled with

$$C_{\text{wall}} = \frac{\epsilon_0 \epsilon_{\text{ox}} w L_{\text{g}}}{t_{\text{ox}}} \tag{3.3}$$

where w is the channel width and L_{g} is the effective length of the channel covered by the electrode.

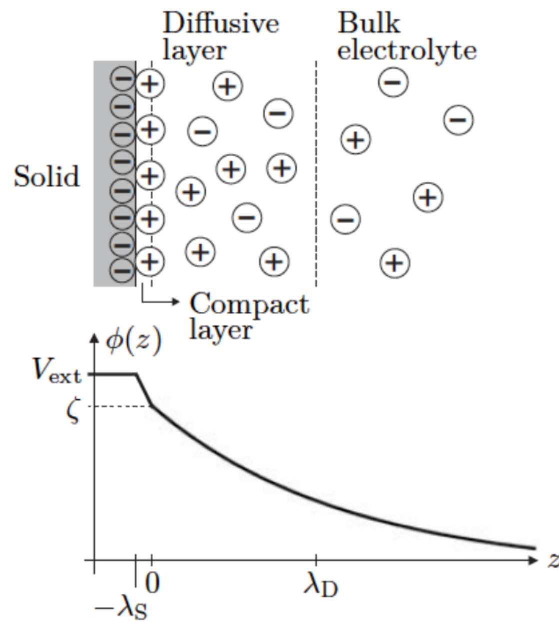

Figure 3.3: Gouy-Chapman-Stern model: ions distribution and potential.

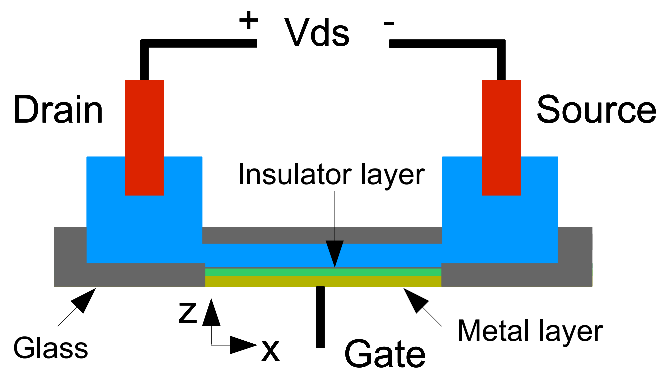

Figure 3.4: FFET device.

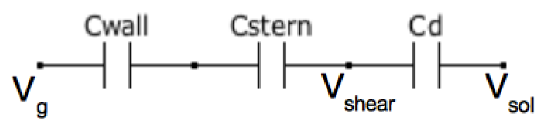

Figure 3.5: Three capacitors model

The diffuse layer is described with an equivalent capacitance

$$C_{\mathrm{d}} = \sqrt{\frac{2z^2e^2\epsilon_0\epsilon_{\mathrm{b}}}{k_{\mathrm{B}}T}N_{\mathrm{A}}1000cwL_{\mathrm{g}}}\cosh\left(\frac{ze}{2k_{\mathrm{B}}T}\zeta\right) \tag{3.4}$$

where ϵ_{b}, N_{A}, c and T are the buffer relative permittivity, the Avogadro's number, the electrolyte concentration in mol/L and the temperature in Kelvin, respectively.

The Stern capacitance C_{stern} is considered constant and usually $C_{\mathrm{wall}} \ll C_{\mathrm{diff}} \ll C_{\mathrm{stern}}$. Since the three capacitors are in series, the effect of the biggest can be neglected and for this reason the model can be simplified in a 2-Capacitors model. The zeta potential is given by the sum of the zeta potential with floating gate and the change created by the gate voltage applied

$$\zeta = \zeta_0 + \Delta\zeta. \tag{3.5}$$

The change in zeta potential is defined as the voltage drop across the diffusion capacitance $V_{\mathrm{shear}} - V_{\mathrm{sol}}$ and can be calculated solving the electrical circuit and obtaining

$$\Delta\zeta = \frac{C_{\mathrm{wall}}}{C_{\mathrm{d}}}\left(V_{\mathrm{g}} - V_{\mathrm{sol}}\right) \tag{3.6}$$

$$C_{\mathrm{tot}} = \left[C_{\mathrm{wall}}^{-1} + C_{\mathrm{stern}}^{-1} + C_{\mathrm{d}}^{-1}\right]^{-1} \approx C_{\mathrm{wall}} \tag{3.7}$$

A most accurate model is the one shown in Figure 3.6. An additional capacitance

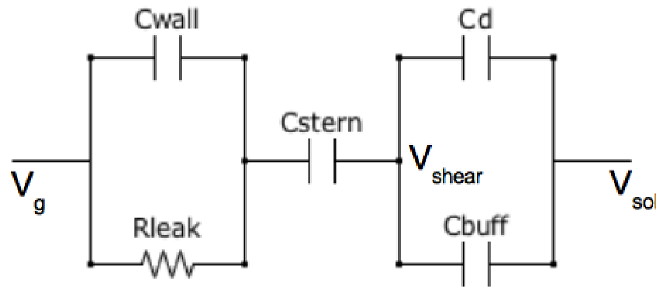

Figure 3.6: Equivalent electrical model used in the simulation: buffer capacitor and leakage resistor.

C_{buff} is added in parallel with the diffusion capacitance in order to consider the effect of the solution pH and a resistance R_{leak} is added in parallel to the oxide capacitance to take account of leakage through the oxide. The zeta potential depends on the pH of the solution because it influences the chemical reactions that take place at the channel walls, in particular the free charges distribution. An important parameter for material used in nanofluidics devices is the point of zero charge (pzc) *i.e.* the pH of the solution that caused a zero zeta potential because there is not an adsorption layer. The zeta potential is positive for $pH < pzc$ and negative for $pH > pzc$. The magnitude increases with $|pH - pzc|$. In our model, the buffer capacitance used for consider the effect of pH on the zeta potential is

$$C_{\text{buff}} = \frac{q^2 \beta}{2.3kT} A \tag{3.8}$$

where β is the number of charged groups on the silica surface per unit area and A is the area. This parameter depends on the the difference between the pH of the solution and the point of zero charge as shown if Figure 3.7, where the fitting curve is obtain from data in [12].

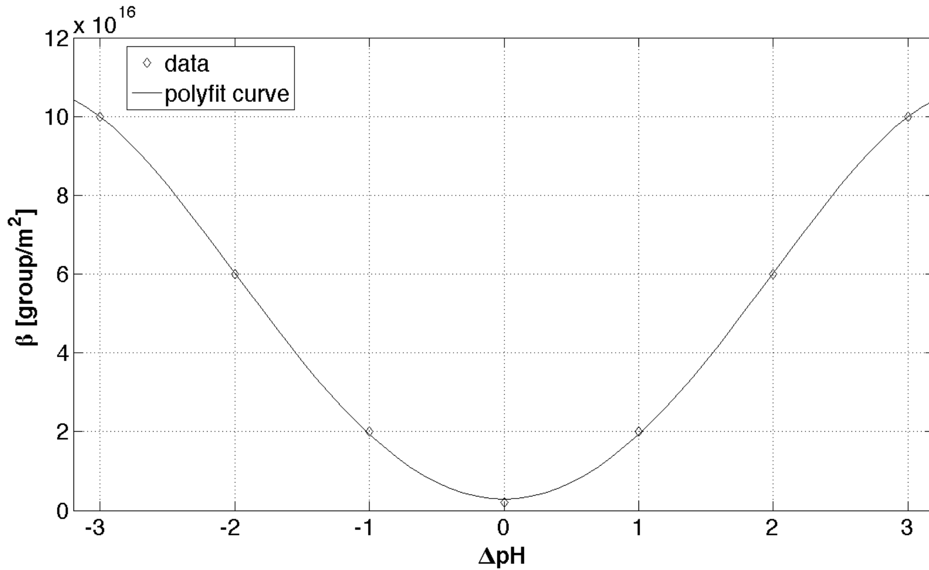

Figure 3.7: Number of charged groups on the silica surface for different ΔpH.

Higher is the ΔpH difference higher is the number of groups and the buffer

capacitance. Since this capacitor is in parallel with the diffusion capacitance, in Equation (3.6) and (3.7) C_{d} should be replaced with an equivalent diffusion capacitance C_{eq}

$$C_{\mathrm{eq}} = C_{\mathrm{d}} + C_{\mathrm{buff}}. \tag{3.9}$$

For this reason, working with solutions whose pH are very different from the pzc of the material caused an increase on the equivalent diffusion capacitance that reduces the ability of change the zeta potential with a gate voltage as stated in Equation (3.6). The leakage resistance is

$$R_{\mathrm{leak}} = \rho \frac{t_{\mathrm{ox}}}{A} = \rho \frac{t_{\mathrm{ox}}}{w L_{\mathrm{g}}} \tag{3.10}$$

where ρ is the resistivity $[\Omega m]$ of the silicon oxide layer deposited above the gate metal. Since the current through this resistance is on the order of the nanoampere, this resistance can be neglected in big channel or high concentration electrolyte (*i.e.* when the current in the channel is in the order of the $10^{-7}A$). Instead, in nanochannel and for low concentration, the current is on the same order of magnitude and the leakage through the oxide has to be considered.

3.2.1 Temperature Dependence

The relation between ζ potential and temperature is complicated and to delve deeper into the issue we suggest [13]. The original ζ potential of the channel increases with the temperature and increases more for high concentration solutions. A first approximated temperature can be derived considering the temperature dependance of the buffer relative permittivity

$$\epsilon_{\mathrm{b}} = 305 \exp\left(-\frac{T}{219}\right), \tag{3.11}$$

that leads to a 1.75% increase per °C on the ζ_0 potential. Moreover, the temperature effects the $\Delta\zeta$ term through the diffusion capacitance as stated in Equation 3.4.

3.3 Distributed Model

Since the potential in the channel due to the external electric field drops linearly, the V_{SOL} in Equation (3.6) is a function of the position x along the channel. This caused a different change in zeta potential that complicated the model of the system. In our work a distributed electrical network is used to describe this effect. The system fluid/oxide/metal is modeled considering a series of N elementary cells shown in Figure 3.8.

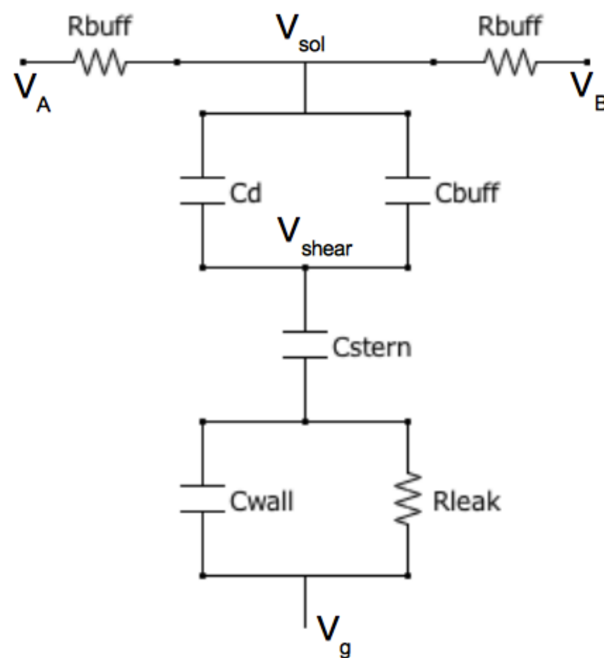

Figure 3.8: Elementary cell for the distributed model.

3.4 Simulation

To investigate the effect of various parameters on the ability of the field effect to cause a change in the ζ potential, a Matlab script used to solve the equation that governed the behavior of a FFET. In particular, the effects of buffer concentration,

solution pH, oxide layer thickness and temperature will be shown in this section. Using data from [14] and [15], values for the ζ_0 are obtained for different steady state situations. That is important because the equations involve this term and if neglected can conduct to wrong results.
As stated in Equation 3.4, diffusion capacitance increases with the square root of the concentration (expressed in mM/L), instead ζ_0 can be approximated with

$$\zeta_0(c) \sim \begin{cases} c^{-1/2}z^{-1}, & \text{when} \quad \zeta \ll 2kT/q \\ a_0 + a_1 pC & \text{when} \quad \zeta \gg 2kT/q \end{cases} \tag{3.12}$$

where pC is defined as

$$pC = -\log{(cz^2)}, \tag{3.13}$$

$a_0 \approx 0$ and $a_1 \approx -10mV$ for silica channels. The ratio ζ/pC is linear for lower pH solution. For basic solution ($i.e$ with $pH > 7$) the ratio reaches a plateau due to the deprotonation of silanoes. The results of Matlab simulations are shown in Figure 3.9 and 3.10 where the variation in the zeta potential and the total zeta potential are calculated, respectively.

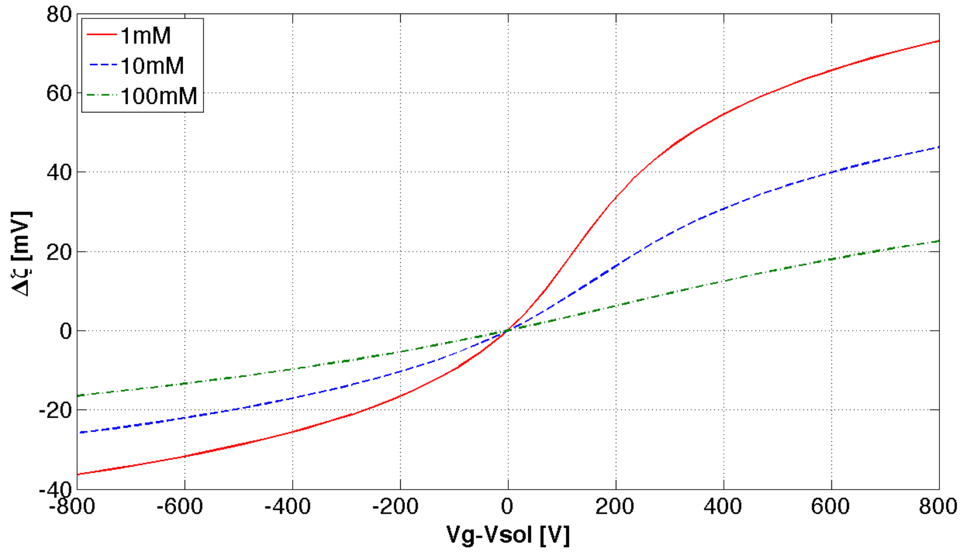

Figure 3.9: Effect of concentration on $\Delta\zeta$.

The insulator layer thickness governs the value of C_{wall} that is proportional to

the $\Delta\zeta$: lower is the thickness higher is the capacitance and higher becomes $\Delta\zeta$ as plotted in Figure 3.11. An important consideration is that the voltage drop across the oxide layer has to be lower compare with the oxide voltage breakdown. For PECVD silicon dioxide the breakdown field is $E_{\text{BD}} \approx 10^3 \quad V/\mu m$ and referring

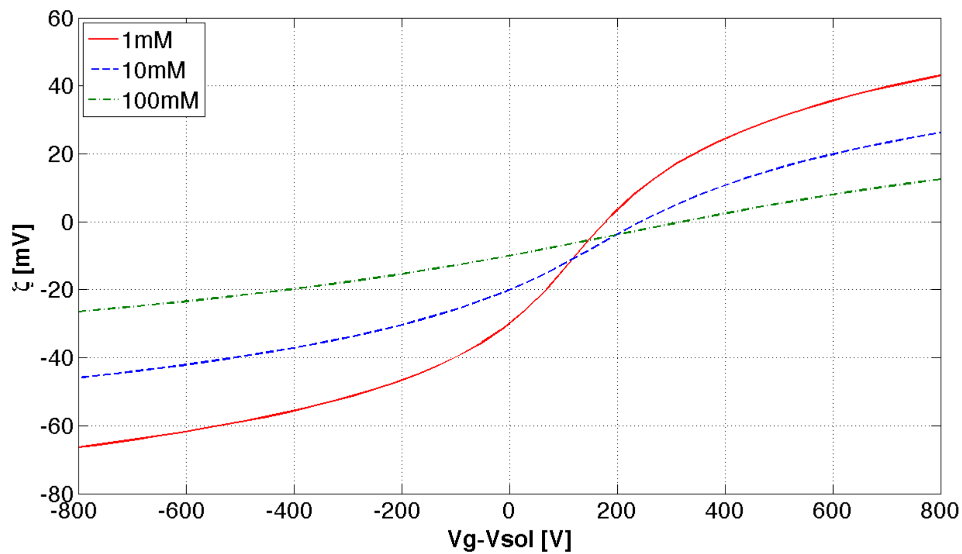

Figure 3.10: Zeta potential for different concentration.

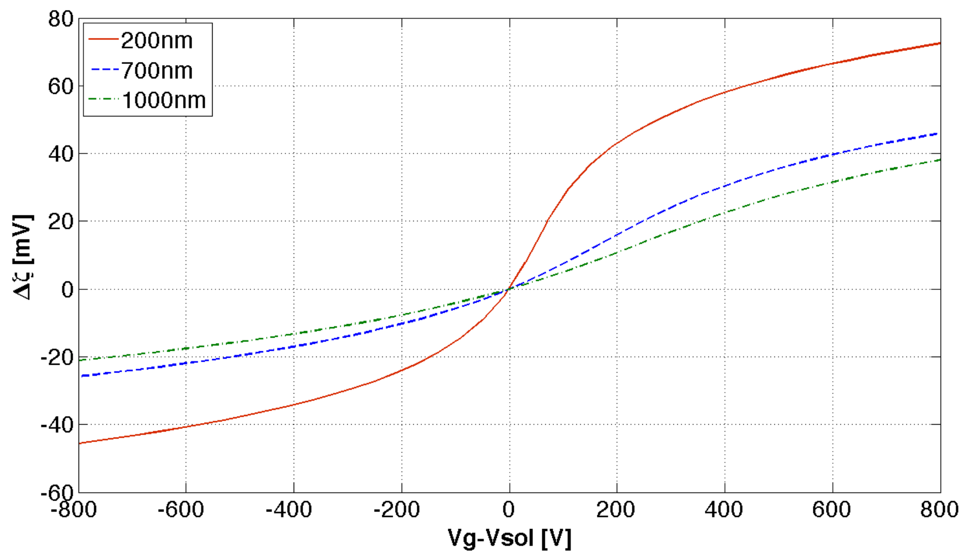

Figure 3.11: Effect of oxide thickness on $\Delta\zeta$.

to Figure 3.11, the curve for the 200nm layer has to be considered valid only in the -200/200V range. Since the insulator capacitance has a great impact on $\Delta\zeta$, other materials either with higher relative permittivity or higher breakdown field should be considered as insulator layer. The temperature effect is illustrated in Figure 3.12 using the assumptions taken in the previous section. The effect on the

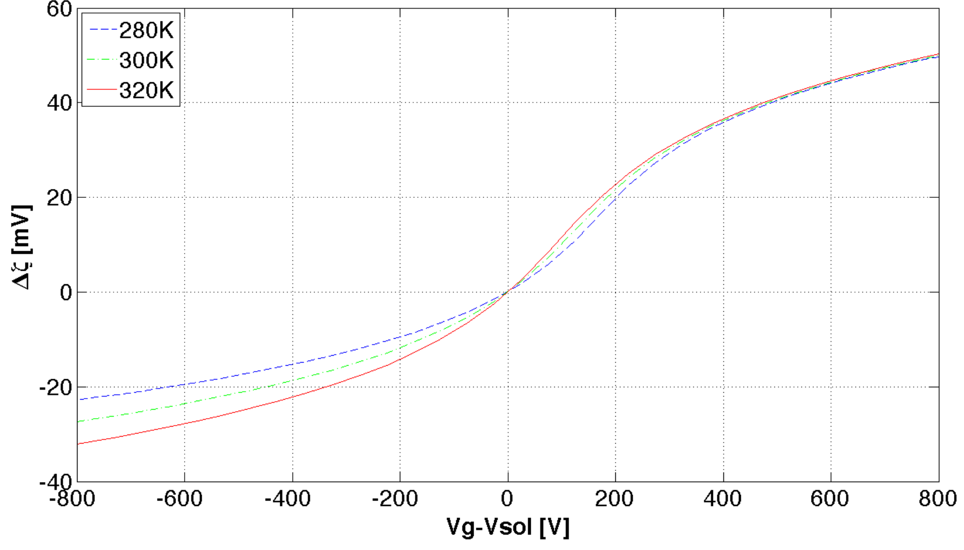

Figure 3.12: Effect of temperature on $\Delta\zeta$.

ζ potential due to the pH of the buffer solution used in the channel are shown in Figure 3.13.

Finally, using the distributed model is possible to observe the different variation in the zeta potential when the linear voltage drop along the channel due to the electrolyte resistivity is take in account. In particular, Figure 3.14 show the simulation results for a $L = 1cm$ long channel with a drain-source voltage of 300 V and a $c = 10mM$ buffer concentration. To reduce the effect of the voltage drop, lower potential difference has to be applied between the two reservoirs. In that case, when the gate voltage is higher enough, $V_{\mathrm{g}} - V_{\mathrm{sol}}$ can be considered independent on the x position and the variation on zeta potential constant.

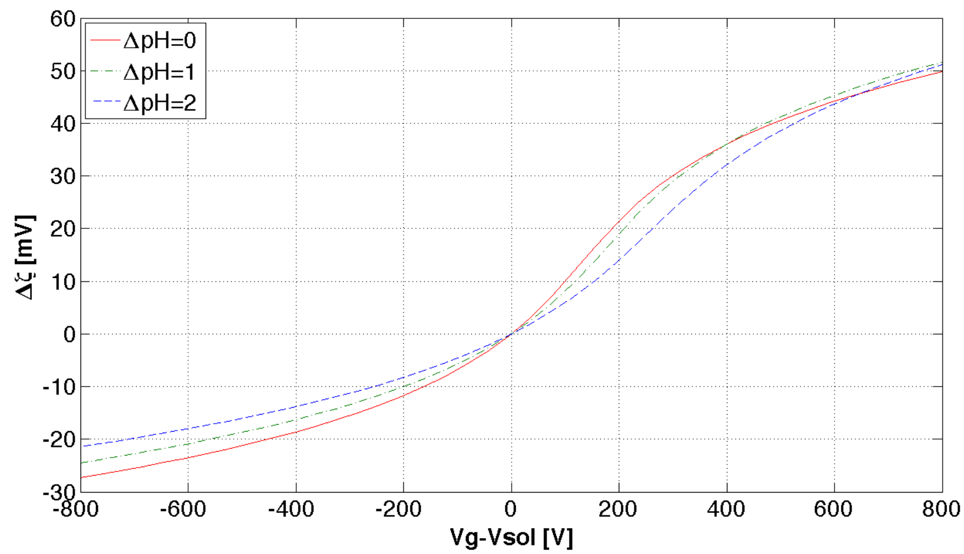

Figure 3.13: Effect of solution pH on $\Delta\zeta$.

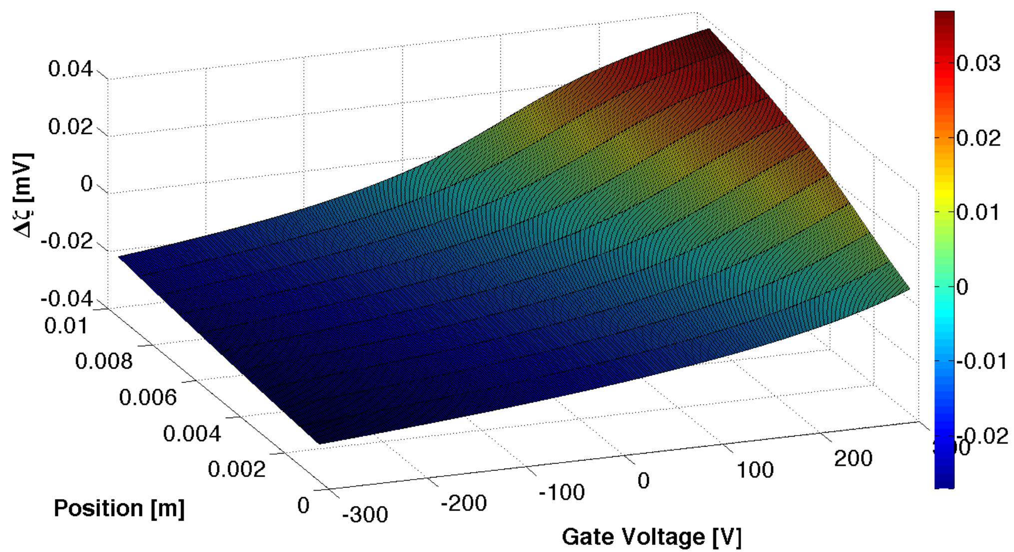

Figure 3.14: Effect of voltage drop along the channel on $\Delta\zeta$.

Chapter 4

Fabrication of microfluidic chips

In this chapter all the techniques used to produce the devices used in the experimental section will be explored. Different methods to assembly molds for PDMS channels will be described as well as the steps to manufacture glass slides with gate electrodes. The fabrication was performed in the UCSB Nanofabrication Facility and in the UCSB Teaching clean room. One chrome mask contain the design for microchannel fabrication shown in Figure 4.1, instead another mask fits the two design for the electrodes deposition as shown in Figure 4.2.

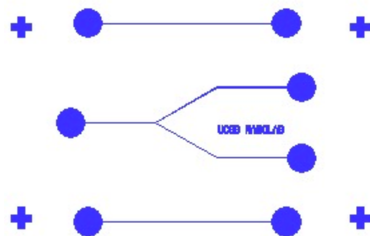

Figure 4.1: Mask for microchannel fabrication.

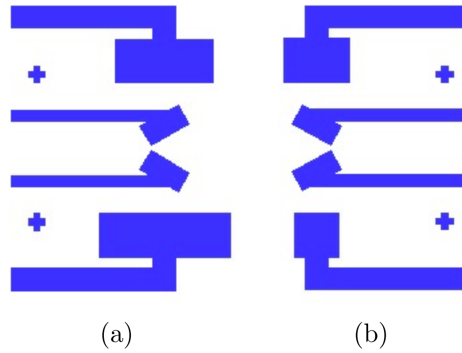

(a) (b)

Figure 4.2: CAD masks for electrodes fabrication process.

4.1 Basic Procedures

4.1.1 Standard Cleaning Procedure

In order to minimize impurities at the surface, the samples have to be clean using the standard cleaning procedure. First, the samples are immersed in a beaker containing Acetone (ACE) and then placed in an ultrasonic cleaner as shown in Figure 4.3. The Acetone is used to dissolve organic materials that may be

Figure 4.3: Ultrasonic cleaner used in the standard cleaning procedure.

present on the surface of the wafers. The use of an ultrasonic cleaner exposes the

acetone to compression waves of roughly (150–400) kHz. This caused a process called *cavitation* which improves the ability of the acetone to remove undesirable particles on the surface. After 3 minutes in the acetone, the samples is removed from acetone beaker and submerged in a beaker of isopropyl alcohol (ISO). The ISO is used in order to remove any acetone left behind. The beaker is placed in the ultrasonic cleaner for another 3 minutes and after that the samples is removed and rinsed in deionized water (DI water) for 3 minutes. The samples are then dried using nitrogen (N_2) gas. This procedure is used throughout the fabrication procedure and will be referred to as the *standard cleaning procedure.*

4.1.2 Lithography

4.1.2.1 Spin of photoresist

Photolithography process is used in order to transfer the design pattern on the samples. After performing the standard cleaning procedure, a dehydratation bake is performed by placing the samples in an oven set a 120 °C for 3 minutes. The wafers are then removed from the oven and allowed to cool down for 3 minutes. The samples are then placed in a hexamethyldisilizane (HDMS) hood for 3 minutes as is seen in Figure 4.4. The HDMS is used as an adhesion promoter for photoresist. To apply the photoresist, the wafer is placed on a turnable chuck shown in Figure 4.5. A vacuum is applied through the holes present on the chuck. A few drops of PR are placed on the center of the chip and then the turnable is turned on to spin a specific rotation rate for a specific time. Setting these two parameters is possible to predict the thickness of the PR layer. Then the sample is placed on the hot plate as shown in Figure 4.6 for a pre-exposure soft bake used to evaporate some solvent from the resist. Minimizing the solvent concentration avoid mask contamination, prevent bubbling of foaming by N_2 during exposure and improve the adhesion to the substrate.

4.1.2.2 Exposure using MJB3 mask aligner

After the pre-bake, the sample is placed on the stage of a Karl Suss MJB3 mask alignment. Referring to Figure 4.7, this mask alignment consists of a sample

Figure 4.4: HMDS treatment used to improve the adhesion of photoresist.

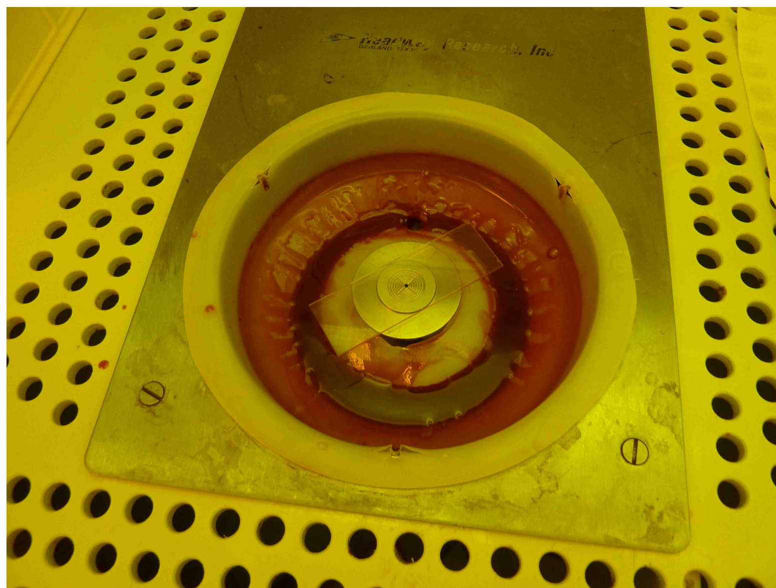

Figure 4.5: Turnable chuck used for spin photoresist on the wafers.

vacuum chuck, mask holder, microscope and exposure source. The exposure source is a mercury (Hg) vapor lamp. This aligner uses the i-line (365 nm), the h-line (405 nm) and the g-line (436 nm) of the mercury lamp. The mask is placed in the mask holder with the chrome side facing the chip. The sample is placed on the chuck and then moved under the mask. After that the chip is moved in the right position using the micrometers for lateral direction, especially if a alignment is needed. After the alignment, the sample stage is moved up to allow the sample wafer to come in contact with the mask. The system is set for an exposure power of 7.5 mW/cm^2. When the exposure is done, the sample stage is moved down and the chip is removed.

4.1.2.3 Post Exposure Bake

A post exposure bake (PEB) can be performed above the softening point of the resist without destroying the structure to be developed due to the still closed resist film. A PEB is applied to reduce mechanical stress formed during softbake and exposure and also to increase the resist adhesion and reduce underetching in following wet chemical etching.

Figure 4.6: Hot plate for pre exposure sof!hbpake and post exposure bake.

4.1.2.4 Developing

To develop the exposed PR (or unexposed in the case of negative PR), the samples are placed in the appropriate developer with mild agitation. The developing time is set to obtain a fully developed pattern on the chip, as can be checked using a microscope. The samples are then rinsed for 1 minute in DI water and blown dry with nitrogen gas.

4.1.2.5 Dektak Measurements

A useful instrument for the test phase is the Dektak profilometer shown in Figure 4.8.

4.2 Mold for PDMS Microfluidics Devices

Polydimenthylsiloxane (PDMS) refers to a group of polymeric organosilicon compounds also known as silicones. This polymer has a repeating $(CH_3)_2SiO$ unit.

Figure 4.7: Karl Suss MJB3 mask alignment used in the lithography process.

PDMS is optically clear, inert, non-toxic and non-flammable. PDMS is used to fabricate microfluidic devices that present mechanical proprieties completely different form glass and silica devices. When prepared, PDMS is a liquid mixture of a silicone and a curing base. The weight ratio between the two components decided the flexibility of the final polymer. In our process, a 10:1 ratio is used to obtain an optimal elasticity of the final devices. The pattern of the microchannels network is transferred to PDMS using a mold where the channels are in high relief respect to elsewhere. Various mold fabrication technique will be explained in this section.

4.2.1 Shrinky Dink Mold

Shrinky Dinks are originally a children's toy kit consisting of large flexible sheets which, when heated in an oven, shrink to small hard plates without altering their color or shape. In particular, a ~ 2.5 times reduction of planar dimensions and ~ 5 times increase in the thickness can be obtain with good repeatability. This proprieties are used to fabricate low quality-low price molds for rapid microfluidic prototyping. With this technique is possible to replicate acceptable channel of

Figure 4.8: Dektak profilometer used in the test step.

$\sim 100\mu m$ width and $\sim 20\mu m$ height. The fabrication steps are:

1. design: the mask that would be replicated is projected with the appropriate dimension to obtain the right channels after the shrink procedure;

2. print: the CAD model is printed on a paper sheet and then transferred on the Shrinky Dinks sheet using a copy machine, to reproduce better the pattern on the transparent plastic;

3. cut: the Shrinky Dinks sheet is then cut with a paper cutter to leave a blank inch around the printed area;

4. bake: preheating a simple toaster oven to 150 °C, placed the plastic sheet ink side up on top of a manila folder, insert in the oven and watch it shrink. When the shrinking process is done, pull out the manila folder and quickly cover the Shrinky-Dink with a blank plastic sheet and a text book to press the mold flat.

The final mold and a profile of the microchannel are shown in Figure 4.9 and Figure 4.10. From the profilometer data is possible to note the trapezoidal shape of the channel, with a $\sim 130\mu m$ minor base and a $\sim 230\mu m$ major base, respectively.

4.2.2 PR Mold

Shrinky Dink molds can be used only for wide devices, due to the limit in the print step. Moreover, to neglect the effect of a rough walls, a width of at least $\sim 100\mu m$ has to be used. To create narrow channel (*i.e.* $\sim 10\mu m$ width), more accurate techniques have to be performed. The simplest consists on the fabrication of a photoresist mold using a simple microscope slide as a support(CORNING ®, $75\times50mm$, $1mm$ thickness). After the standard cleaning procedure described early in this chapter, a lithography procedure is performed with Clarient ® AZ4110 positive photoresist. The fabrication steps are:

1. standard cleaning procedure;

2. HMDS deposition;

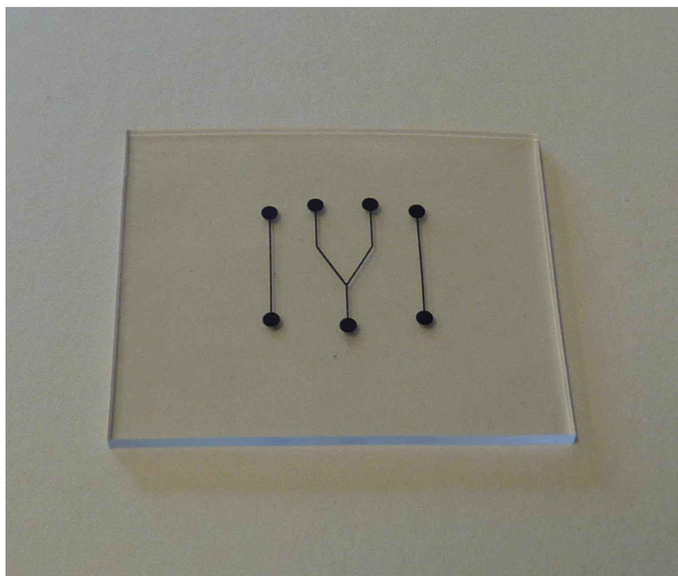

Figure 4.9: The final Shrinky Dink mold used for replicate microchannels.

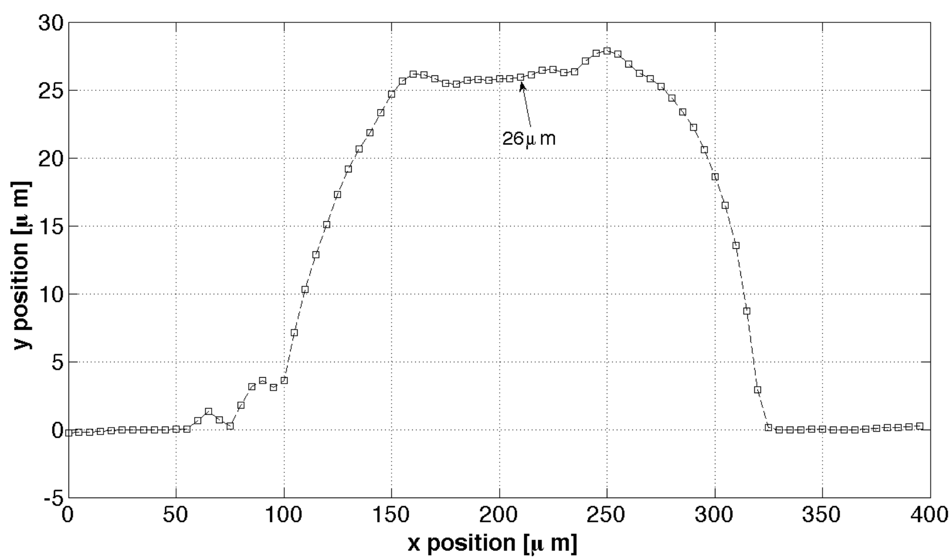

Figure 4.10: A cross section profile of the Shrinky Dink mold obtain with Dektak.

3. PR spinning: spin of AZ4110 at 3500 rpm for 30 seconds;

4. softbake;

5. exposure: 20 seconds at 7.5 mW/cm^2;

6. PEB: 5 minutes post exposure bake at 110 °C to improve mechanical resistance of resist;

7. developing: the glass slide is soaked in a solution of 4:1 DI water and Clarient ® AZ400K developer for 60 seconds with mild agitation, followed by a 1 minutes water rinse.

Figure 4.11 shown a particular of the Y junction in the PR-mold. The shadow on the channel walls is due to the non-sharp profile of the photoresist. This is proved analyzing the profilometer data provided in Figure 4.12. The top width is $6\mu m$, instead the bottom width (on the glass surface) is $20\mu m$. The heigh of the channel is $1.25\mu m$. This trapezoidal shape is caused by the incorrect exposure time that has to be increased to obtain a more accurate lateral profile. The process was not repeated because the heigh is still the lower dimension and this is the condition used in the current simulation.

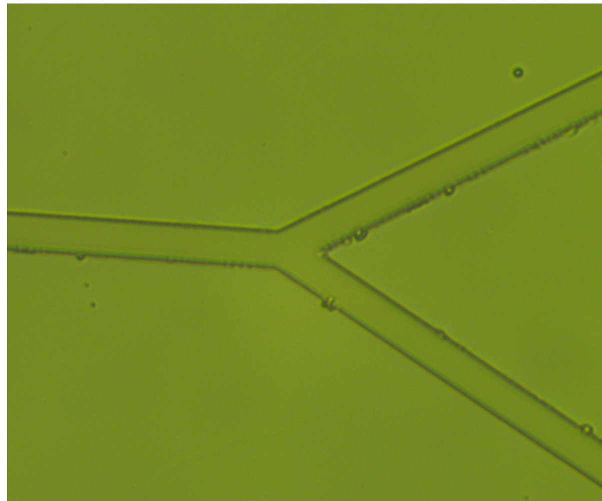

Figure 4.11: A microscope picture of the PR-mold Y junction.

4.2.3 Glass Mold

Starting from the photoresist mold is relatively easy to produce a more durable mold for PDMS microchannels fabrication. In the PR mold the photoresist is covering the area where the channel will be created, and it acts as a mask. The glass slide is wet etching in FUJIFILM ®Buffered Oxide Etchant, a silicon oxide etchant formulated from high purity 49% Hydrofluoric Acid and high purity 40% Ammonium Fluoride. A 10:1 NH_4F:HF ratio solution a 20 °C is used to etch the glass not covered by the photoresist. The slide is rinsed with DI water for 1 minute and then soaked for the desired time in the BHF solution followed by another 1 minute DI water rinse. The etched glass is then soaked in acetone to peel off the undeveloped photoresist and rinse again with DI water. The etch rate for soda lime glass is considered faster that for thermally grow silicon dioxide due to the amorphous lattice structure of the first material. Three different profilometer profiles for three different etching times are shown in Figure 4.13 and from these data a etching depth vs etching time is presented in Figure 4.14. The etch rate can be derived from the slope of the linear fitting curve as $1.13\mu/min$.

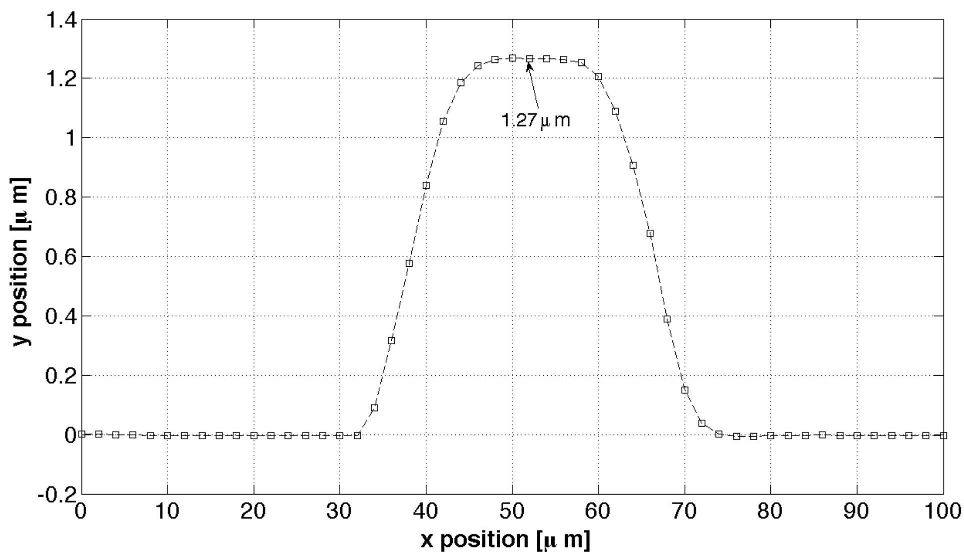

Figure 4.12: A cross section profile of the photoresist mold obtain with Dektak.

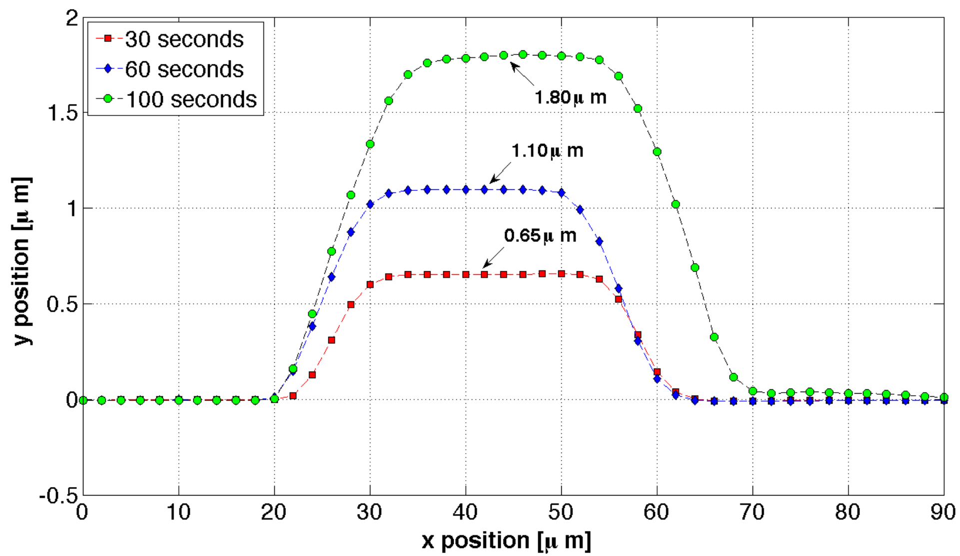

Figure 4.13: Dektak profiles of glass molds for different etching time.

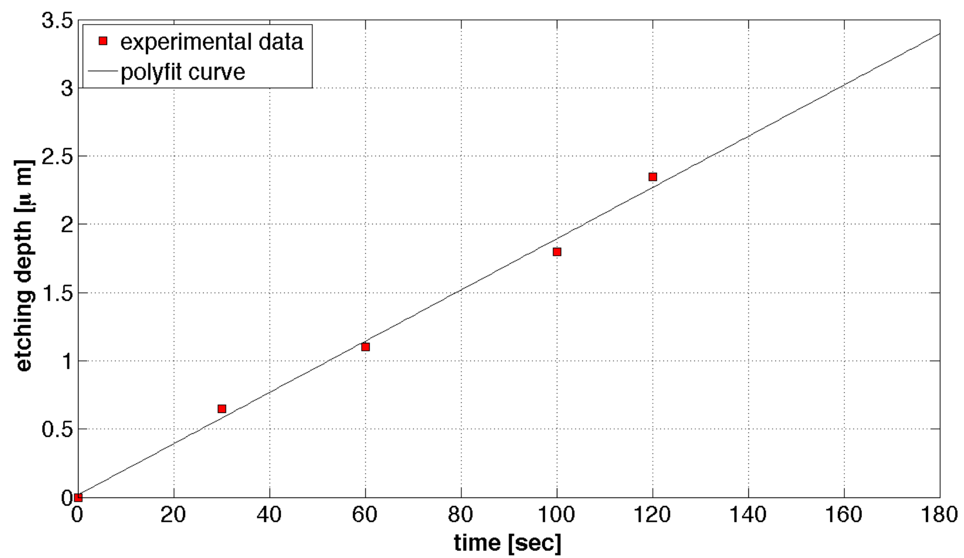

Figure 4.14: 10:1 BHF etch rate for soda lime glass.

4.2.4 Silicon Mold

Silicon mold fabrication involved more steps than other techniques but has the advantage to use silicon, a very well known material for microfabrication.

4.2.4.1 Oxidation of silicon wafer

After the standard cleaning procedure, in order to minimize the impurities contained in the oxide that has to be grow, a *piranha clean* is performed. A solution of five parts sulfuric acid (H_2SO_4) and one part hydrogen peroxide (H_2O_2) is heated to 100 °C. While keeping the solution at this constant temperature the wafers are submerged for ten minutes. Then the samples are rinsed in DI water for two minutes and dried with nitrogen gas. The mixture is a strong oxidizer and an oxide layer grows naturally during the cleaning procedure. In order to have a precise control of the thermally grown oxide, this undesired layer has to be removed. The wafers are dipped in 50:1 DI H_2O:HF (hydrofluoric acid) for one minute. Finally the samples are rinsed again in DI water for two minutes and dried with nitrogen. A thin layer of silicon dioxide (SiO_2) has to be grown to serve as a protective layer during the KOH etching step described later. This film is grown in a thermal oxidation furnace shown in Figure[4.15]. This furnace walls consist of a quartz cylindrical tube. On one end of this tube there is a small inlet opening that allows for nitrogen gas, oxygen gas and water vapor to be delivered into the furnace. Heating elements surround the quartz tube in order to ensure uniform temperature inside the oxidation chamber. When desired, wafer vapor can be supplied to the furnace via a boiler process. The boiler consists of a vertical cylindrical chamber. A DI water drip supplies the water to be boiled. An electrical heating element surrounds the outside of the boiler chamber. This boiler has a gas exhaust feed that connects to the gas inlet at the back of the furnace allowing for the transport of water vapor. The furnace is set to remain at a constant 1000 °C. After the final temperature is reached and the water in the boiler is boiling, the valve for the nitrogen gas supply is closed and the one for the oxygen gas supply is opened and oxygen gas flows into the furnace. The samples are loaded on a quartz sample tray (boat). The boat is placed at the mouth of the furnace for 2 minutes and then slowly pushed in over a period of 3 minutes till the central zone is not reached. The

Figure 4.15: Furnace used to grow thermal oxide on a silicon wafer.

wafers are left for 2 minutes to heat up to the furnace temperature. A dry oxide is then grown in the O_2 gas for ten minutes. This first 60 Å layer ensures a better final quality of the oxide, because the interface between silicon and dry oxide is better than the one between silicon and wet oxide Then the oxygen valve is closed and the water vapor process is turned on. Under these conditions a wet oxide is grown for 87 minutes. This time is derived from the Deal-Grown model [16] in order to grow a 500 nm oxide layer. Then the water vapor process is turned off and the oxygen valve is open. Another layer of dry oxide is grown for 10 minutes. The oxygen valve is closed and the nitrogen valve is opened. The boat is slowly pull out of the furnace over a span of 3 minutes and then it is left at the mouth of the furnace for 2 minutes. At this point the boat is removed from the furnace and left to cool to room temperature on a quartz pad. The real oxide thickness can be check in different methods:

- color chart;
- ellipsometry;
- reflectance measurement.

The most accurate data is achieve with the last one, that was performed with Filmetrics(name of instrument) and gave a thickness of 5100 Å.

4.2.4.2 Etching 50:1 HF

After the oxidation step, the photolithography procedure is performed to define the design pattern in the silicon wafer. Following the steps present at the beginning of the chapter, AZ4110 positive photoresist is spin for 30 seconds at 4000 rpm. Then the sample is placed in the mask aligner,exposed for 20 seconds at 7.5mW/cm^2 and then soaked in the AZ400K resist developer for 1 minute. At this point the photoresist is remained only where the channels will be created. This photoresist pattern is used as a mask for etching the oxide everywhere except where the resist covers the wafer. A solution of 50:1 H_2O:HF is used. The etch rate for SiO_2 is between (45–65) Å/min at 21 °C. Instead, the etch rate for photoresist is several orders of magnitude lower and that allowed to use it as a hard mask. The chip is immersed in DI water for 1 minute in order to prevent bubble formation and

ensured uniform etching in HF. Then the samples are placed in the HF solution for the time required to etch all the oxide not covered by the photoresist. Then the PR is stripped using a standard cleaning procedure.

4.2.4.3 KOH Etch

Potassium hydroxide (KOH) etches 100 Silicon anisotropically with an angle of 54.7 °with a very high selectivity to SiO_2 (about 1000:1 at 20% concentration at 80 °C). A 20% KOH solution is prepared by diluting 45% KOH solution with DI water. The final solution is heated up to 80 °C on a stirring hot plate. The samples are placed on a Teflon boat and then immersed in the KOH solution. Using data from Figure[4.16], the etch rate in these conditions is 87 µm/h and for a target depth of 5 µm, the required time is 3 minutes and 40 seconds. Different etch rate

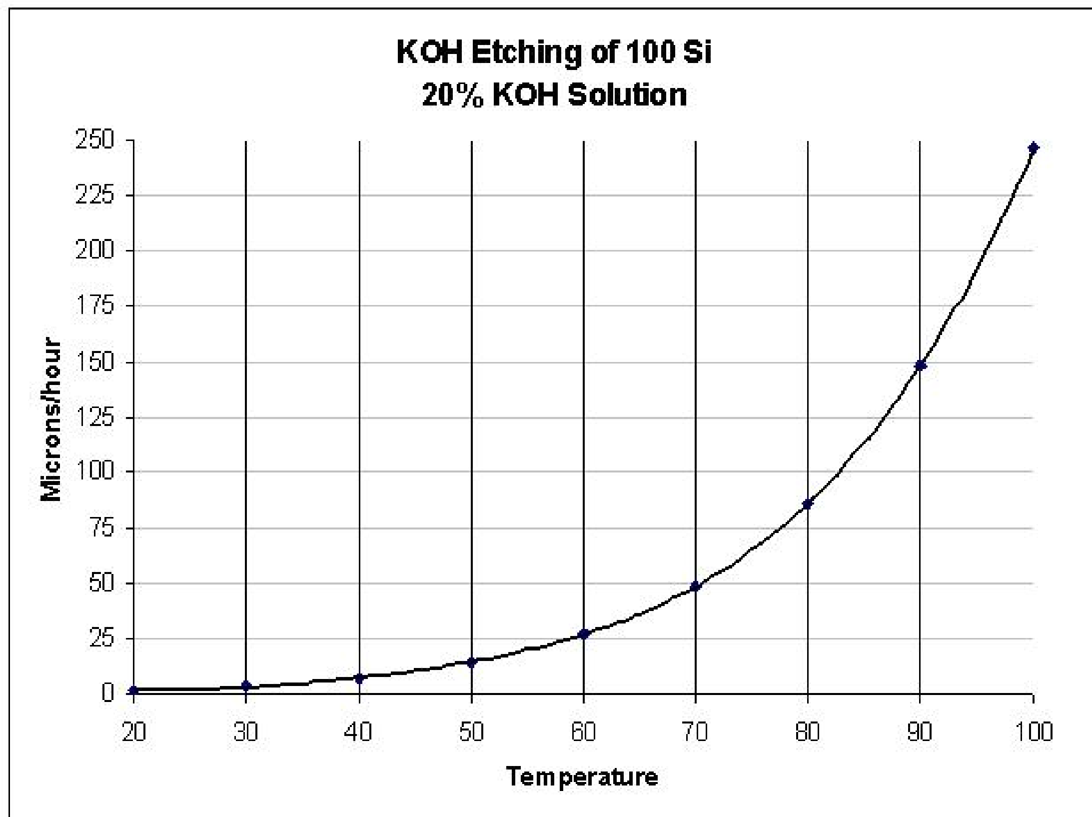

Figure 4.16: KOH etch rate of 100 Si for a 20%KOH solution.

curves are obtained for different KOH concentrations and silicon orientation plane [17],[18]. At the end of the etching the boat is removed from the KOH solution and rinsed with DI water for 1 minute and then the samples are blown dry with N_2. The silicon mold for the polymer microchannel fabrication is complete.

4.3 Fabrication of gate electrodes on glass

To build a device suitable for the Field Effect Flow Control, a metal electrode insulated form the fluid has to be construct. In this section we will go through the procedure to realize the bottom side of our microfluidic device. During the fabrication, three metallization were performed to solve several problems encountered. The first set of slides consist only in a titanium-gold deposition followed by the silicon dioxide PECVD (*Plasma-enhanced chemical vapor deposition*). The other two sets consisted on a BHF wet etching, metal deposition and PECVD. In particular on the second only titanium was deposited, instead on the third set a titanium-gold-titanium sandwich was created.

4.3.1 Cleaning and photolithography

The fabrication of electrodes on a glass slide follows the procedure used for the silicon chips. The glass slides are cleaned using the standard cleaning procedure. Then a dehydration bake is performed for 3 minutes at 120 °C. The slides are then removed from the oven and cooled down for 3 minutes. The samples are then placed under HMDS hood for 3 minutes. AZ4110 positive photoresist is spun on the samples at 4000 rpm for 30 seconds followed by a softbake at 95 °C for 1 minute. Then the samples are exposed to UV light on the MJB-3 aligner for 20 seconds. The slides are then immersed in 4:1 DI H_2O:AZ400K solution for 1 minute in order to develop the photoresist and then rinsed in DI water for 1 minute. After blown dry with N_2 the samples are ready for the direct metal deposition or for a wet etch step.

4.3.2 Trench etching

In the first set of glass slides, a metal evaporation process was direct performed. Instead, an intermediate step was implemented for the other two sets of slide. To obtained a final electrode slide as flat as possible, the slide patterned with the photoresist is BHF wet etched. Trenches are created where the metal has to be deposited. The depth of the etch allowed to fit the metal layer(240nm) and a thin oxide layer($\sim 100nm$). The other oxide will cover all the slide and with a CMP(*Chemical Mechanical Polish*) will be possible to make flat the surface.

4.3.3 Metal evaporation

The metal evaporator used in the clean room is a Load Locked Metal Evaporator Dual Gun shown in Figure 4.17. The system allows very quick cycle time for evaporation (as low as 20 minutes total time). The front gun contains metals Ti, Pt, Ni, Au and the back gun contains metals Pd, Al, Ag, Ge. These metals stay under high vacuum at all times, except during maintenance, to maintain source purity. One wafer up to 4" diameter or multiple pieces can be placed into this system for evaporation. There is also a special fixture that can be inserted for angling and/or rotating the sample during deposition. This system is used for n-type ohmic contact metallization to compound semiconductors, Schottky contacts to semiconductors, bond pads, and other general metallization. The maximum deposition thickness during a run is limited to $1\mu m$.

The slides are placed on the chip holders and blown dry with N_2. The chip holders are inserted inside the vacuum chamber. The vacuum pump is turned on and set for a target pressure of 1×10^{-7} Torr. Once this pressure is reached, the desired metal layer is deposited with a deposition rate of 5 Å/s. If an additional metal layer is needed, the system is first cooled down for 10 minutes and then the new film is deposited. Finally, the system is cooled down for 10 minutes and then the glass slides are removed from the chip holders. The proprieties of the three slide sets are listed in Table 4.1.

(a) Metal evaporation machine

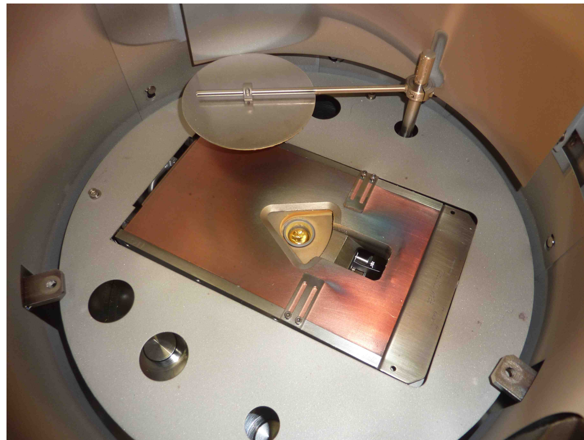

(b) Particular of the beam inside che chamber

(c) Chip holders inside the metal evaporator chamber

Figure 4.17: The metal evaporator system used for depositing metal on the glass slides.

4.3.4 Metal lift-off

The acetone strip off the photoresist. If a metal layer is above the photoresist and the solvent is able to etch the resist layer, also the metal is stripped away. This process allowed to keep the metal only where there is not photoresist on the sample. This technique used to remove metals is called *metal lift-off*. After the metal deposition, the samples are immersed in acetone for 2.5 h and to facilitate the lift-off of the metal the slides are shaken gently. When the metal is completely stripped off, the samples are placed in isopropanol for 2 minutes to remove acetone and then rinse with DI water for 2 minutes. Then the samples are blown dry with N_2.

4.3.5 PECVD oxide deposition

After the metal lift-off, the slides are cleansed with the standard cleaning procedure to avoid the presence of contaminants on the sample surfaces. This is necessary to perform an uniform silicon dioxide deposition. The oxide cannot be grow thermally for the presence of the metal. Oxide can be obtain a lower temperature compared to the melting point of the metals but the thermal stress can caused defect on the conductive path and adhesion problems. For these reason, the silicon dioxide is deposited through PECVD using the PECVD Plasma Therm 790 shown in Figure 4.18. The deposition chamber is cleaned for 30 minutes with CF_4 gas and then 200 nm of SiO_2 are deposited everywhere. The slides are then placed in the chamber and create vacuum. Once the required pressure is reached, a 8000 Å SiO_2 layer is deposited in 19'25"8. The deposition parameters are listed in Table 4.2, 4.3 and 4.4.

Set #	Metals
1	500 Å Ti + 500 Å Au
2	2400 Å Ti
3	500 Å Ti + 1400 Å Au +500 Å Ti

Table 4.1: Metal layers in the three sets of slides used in the experiments.

Figure 4.18: PECVD Plasma Therm 790 for Oxides and Nitrides deposition.

RF Generators Power [W]	
RF power	22
Ref	0
DC	28.22

Table 4.2: PECVD generators

	Gas Chambers	
	SET POINT	ACTUAL
SiH_4	100	97
N_2O	300	300

Table 4.3: PECVD machine

4.3.6 Electrodes vias

To open windows through the oxide layer to contact the metal electrodes, a hand-made mask is prepared. After the standard cleaning procedure, AZ4110 positive photoresist is spin on the slide. Using a precision paper cutter,holes are cut on a thin aluminum foil. That sheet wraps the slide and the holes are aligned with the metal paths. The slide is then expose using MJB3 mask aligner and than soaked on the photoresist developer for 1 minutes. The slide is then dipped in BHF solution for 5 minutes to etch the 500nm of silicon dioxide. A ohm-meter is used to check the correct connection with the metal.

4.3.7 Chemical Mechanical Polishing

Chemical Mechanical Polishing is a process that is used to minimize the surface topography. In our device fabrication, this technique is used to prepare the slides with the electrodes for a better bonding with polymer and for a possible glass/glass device. After a hot plate is heated up to 235 °C, the chip holder shown in Figure 4.19(a) is put on it and a crystal bonding glue is melted on the top of this ceramic plate. Once melted, the glue is smoothed with a razor blade to create a thinner layer. The plate is then put for 10 minutes in the pressure machine shown in Figure 4.19(b) to make flat the glue film. Then the slides are placed above this film and another clean ceramic plate cover with a weighing paper is set on top. The two plates are then left in the pressure machine for 30 minutes to allocate the slides as flat as possible. A polishing slurry solution is heated to 35 °C and then the place with the slide is set down in the CMP machine illustrated in Figure 4.20. In our set up, the central plate rotates at 60.6 rmp instead the left plate (the one

	data	
	SET POINT	ACTUAL
Temperature channel 2 [K]	294	293
Pressure [mT]	900	900

Table 4.4: PECVD data

with the slides) spins at 20.6 rpm. Using a glass slide etched in BHF, checking at the channel cross section profile with a Dektak, the removal rate is estimated in 160 nm/s.

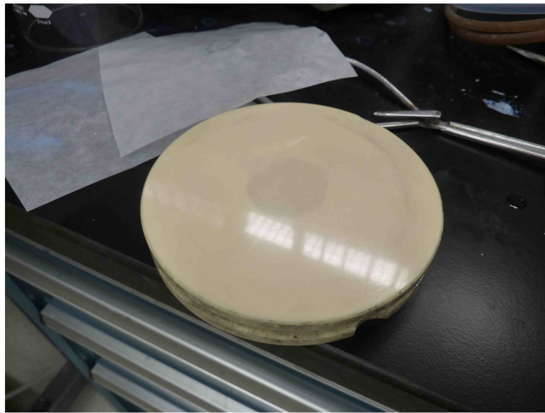

(a) Device holder

(b) Pressure machine

Figure 4.19: Particular of the device holder and of the high pressure machine.

Figure 4.20: Lapping machine used during CMP procedure.

4.4 Microchannel fabrications

4.4.1 Glass microchannel

To etch microchannel in microscope glass slide we use the mask shown in Figure ??. In this chrome mask the dark area is the pattern to transfer to the glass. To etch this region, a negative photoresist has to be used as a soft mask. After the standard cleaning procedure, AZnLOF2020 negative resist is spin for 30 seconds at 3000 rpm, followed by 90 seconds softbake at 110 °C a 9 seconds exposure and a 90 seconds PEB at 110 °C. To develop the resist, the slides are soaked in AZ300MIF for 60 seconds. Then they are sunk in BHF and then rinsed with DI water, obtaining the following channel depth:

- 120 seconds BHF: 2.33μm;
- 85 seconds BHF: 1.7μm.

In Figure 4.21(b) and 4.21(a) are visible the effects of the BHF wet etching on the glass slide. The edges are not good defined due to the presence of other compounds in addition to the silicon dioxide, as stated in Table 4.5.

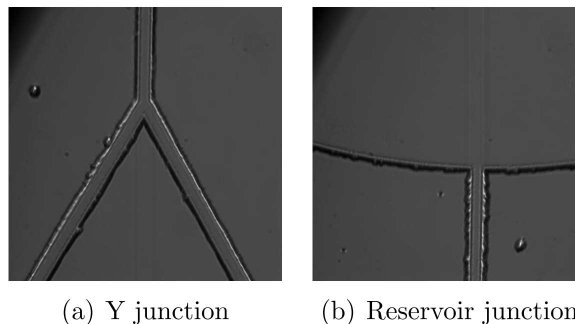

(a) Y junction (b) Reservoir junction

Figure 4.21: Microscope images of glass etched microchannel.

4.4.2 PDMS microchannel

4.4.2.1 Silicon and glass molds preparation

The silicon chips and glass slides are used as molds to obtain a PDMS-based microfluidic system. (tridecafluoro-1,1,2,2-tetrahydrooctyl) trichlorosilane (further

referred as silane for abbreviation), purchased from Gelest,Inc(Morrisville, PA, USA), is used in the PDMS molding processes as a release agent to reduce the adhesion of PDMS to the molds by making a monolayer on the molds surface prior to the casting of the PDMS component.The cleaned mold is placed on its flat side inside a sealable container such that the features remain on the top. Few droplets (e.g. 10 droplets for a 1 L container) of are placed around the sample. The container is then covered and sealed by placing the lid at ambient. The silane is evaporated until the equilibrium is reached inside the closed container. The sample is therefore exposed to the vapor. After a certain amount of exposure time the lid is removed at a ventilated place and the sample is taken out [19]. After that the outside of the mold is wrapped with fiber tape or with a tinfoil to create a border.

4.4.2.2 PDMS preparation

PDMS is obtained from a mixture of Sylgard ® 184 Silicone Elastometer Base and 184 Silicone Elastometer Curing Agent. The weight ratio of the two substances decide the flexibility of the final polymer. In our case, a medium pliable compound is reached with a 10:1 ratio. For the dimension of our molds, around 10 g of Sylgard 184 silicone base is put in a plastic mixing dish and then the curing agent is added at 10% of the weight. The content of the dish is mixed vigorously and then is poured into the taped mold until a layer of ∼4 mm. The silicon mold with liquid PDMS inside is vacuum chambered to eliminate the bubbles in the mixture. That

Chemical Compound	Percentual [%]
Silicon Dioxide	72.20
Sodium Oxide	14.30
Calcium Oxide	6.40
Magnesium Oxide	4.30
Aluminium Oxide	1.20
Potassium Oxide	1.20
Sulfur Trioxide	0.03
Iron Oxide	0.03

Table 4.5: Chemical composition of microscope slides (Fisher Brand).

ensures better surface geometry on the final device and also a clear view of the channels for microscope inspection. After the bubbles have been removed from the PDMS, the mold is placed in a preheat oven at 65 °C. The PDMS is cured for 4 hours. Once is done, the mold is cooled down and the tape is removed from the mold and the PDMS is gently peeled off. The rounded edges of the PDMS are cut off to increase the flatness of the device. After that step, access holes in the PDMS are punched using Biopsy punch. The PDMS chip is then rinsed with acetone, isopropanol alcohol and DI water. The PDMS cannot be soaked in any substance (except water) because it absorbs ions that modify its surface proprieties.

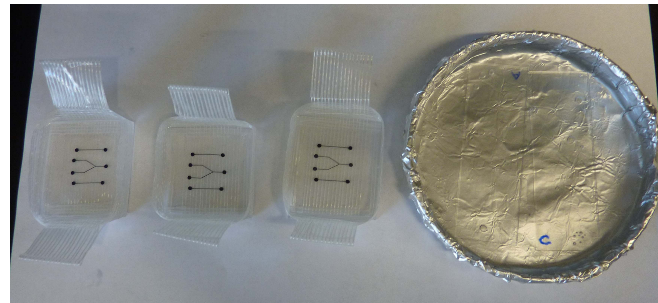

Figure 4.22: Liquid PDMS cast in the Shrinky Dinks and glass molds.

4.5 Bonding

The last step of the microchannel devices fabrication is the bonding between the slide with the metal electrodes and the one with the micropatterns. Through this section we will explain the two different bonding tried during the thesis.

4.5.1 Glass-PDMS Bonding

The clean PDMS surface is treated with the plasma bonder shown in Figure 4.23. After the bonder is calibrated, it is slowly run for 10 seconds over the PDMS channel side and arcing it will occur. This ensures optimal bonding proprieties and hydrophilic characteristics. Then the PDMS is aligned with the electrodes on

the glass slide and using hand pressure the two parts are bonded together. The final devices are illustrated in Figure 4.24 where the channels are marked in red.

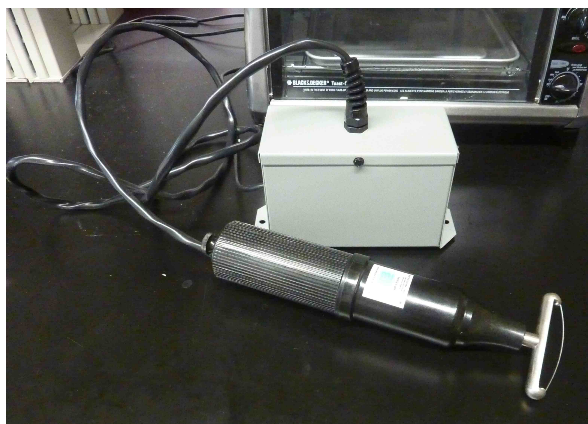

Figure 4.23: Plasma bonder used in the PDMS-glass bonding.

Figure 4.24: Final PDMS-glass devices.

4.5.2 Glass-Glass Bonding

A glass-glass bonding was tested but not good results were obtained. In a microscope slide where channels was etched, holes to contact the reservoirs are drilled. To eliminate possible defects from the drilling process, the slide is CMP for 5 minutes to obtain a very flat surface. The electrodes and channels slides are ultrasonic cleaned for 1 hour in order to remove all the residual from the CMP step. The two slides are then soaked in a piranha solution for 10 minutes. Piranha cleaning is used to remove carbon from the surface and due to its high acidity, it also dissolves deposits such as metal oxides and carbonates that are present in the soda lime glass used in microscope slides as listed in Table 4.5. Then a 30 seconds BHF wet etch is performed to remove the oxide layer that formed during the piranha treatment, followed by another 8 minutes piranha cleaning. The two slides are then rinsed with water and blow dry with N_2. Then they are flipped one over the other and gently pressed together. A good pre-bonding is obtained and no Newton rings are visible. The channel were filled with water and no leakage was present. Using fused silica it is possible to obtained better bonding due to the lattice regularity but higher temperature ($\sim$1600 °C) has to be reached. This requirement is not compatible with the presence of the metal on the slide. Soda lime glass has a lower softening temperature(720 °C) compared to fused silica(1665 °C), so the bonding process is suitable. The device was placed in the oven and a 50 °C step increase every 15 minutes was performed. Once the oven reached 600 °C, the temperature was keeping constant for 1 hour and then cool down to 100 °C in 10 hours. The final device did not work. The glass surface cracked and leakage occurred when the channels were filled with water. Possible reasons from the bonding failure can be related with chemical reactions that took place at high temperature. Future direction to avoid this problem will be bonding the slides at the annealing point(545 °C) instead of softening point.

Chapter 5

Measurement of EOF and FEFC

5.1 $2pK$ model simulation

Using the Matlab script prepared K. L. Jensen and J. T. Kristensen and described in [8], simulation for the electromigration and advection currents are obtained for different concentration of the Sodium Acetate Buffer used in the following experimental sections. In particular the Debye length decreases with the concentration as shown in Figure 5.1. Referring to Equation 2.24 and 2.28, the ratio between advection and electromigration currents is always small as shown in Figure 5.2. Here the ratio is plotted respect the ratio between the channel height and the Debye length. With these considerations, when we measure the total current through a microchannel, we can assume that we are measuring the electromigration current.

5.2 Fluid Flow in the Microchannel

Using the numerical model prepared by A. Lenzi and F. Viola, the movement of the fluid can be studied. Specifically, the model studies the behavior of the liquid when a discontinuity in the zeta potential is present on the channel walls. Since with the electrical model presented in Chapter 3 is possible to related the gate voltage to the $\Delta\zeta$, with the numerical model the field effect can be associated with the movement. Since in our channels only one wall is covered with the metal, only

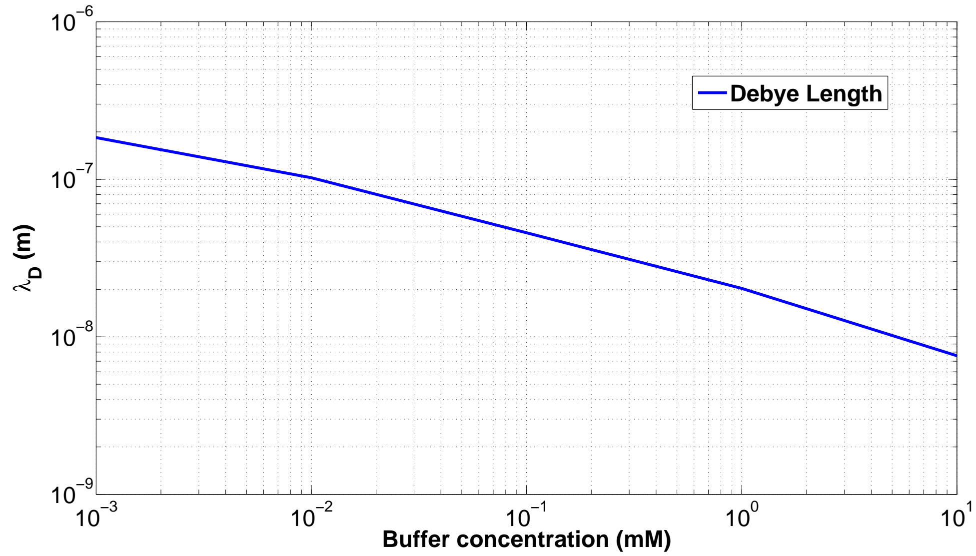

Figure 5.1: Debye length as function of concentration.

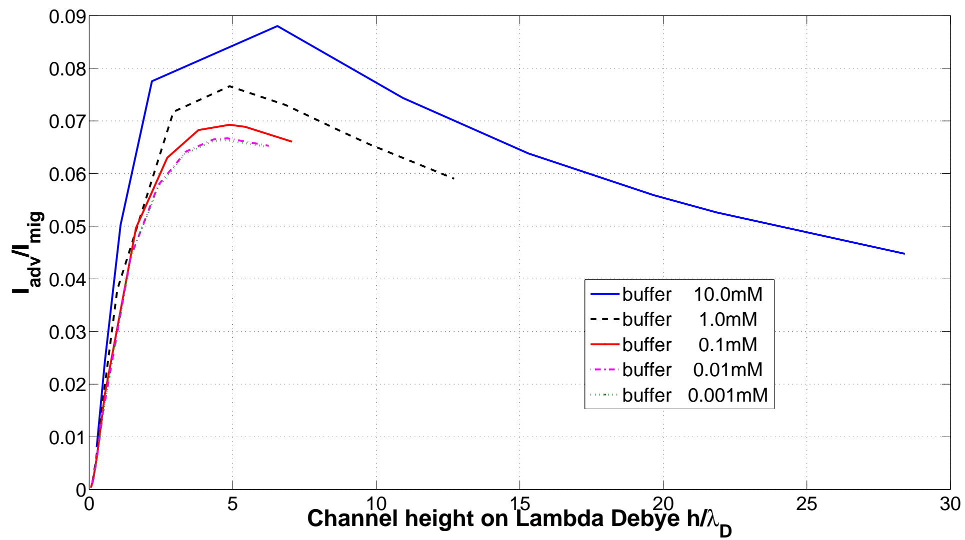

Figure 5.2: Ratio between Electromigration and Advection currents.

one side is effected by the gate voltage leading to asymmetric situation. For this reason, the electroosmotic velocity cannot be derived from the new zeta potential but the flow has to be solve taking in account also the boundary conditions implied by the areas of the channel not covered with the electrode. Figure 5.3, 5.4 and 5.5 show the results of Matlab simulation for a channel with a step discontinuity in the zeta potential. In particular, the zeta potential is ζ_1 everywhere excepted for the bottom right area where is $\zeta_2 = -\zeta_1, -3\zeta_1, -9\zeta_1$. To reverse the flow, an

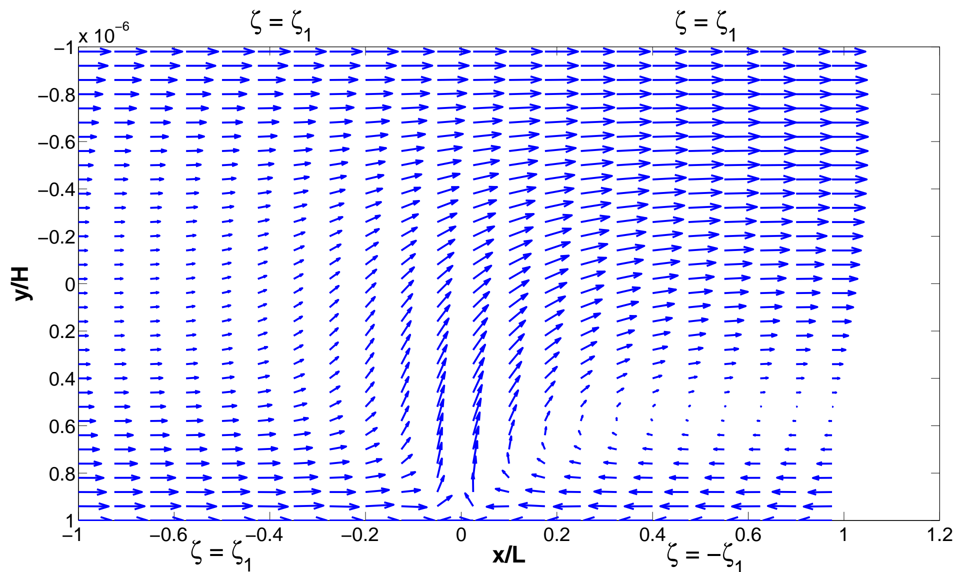

Figure 5.3: Velocity field with $\zeta_2 = -\zeta_1$.

higher zeta potential in the metal area is required compared with the one predicted by the electrical model and using the simple Smoluchowski's equation 3.1.

5.3 Current monitoring measurements

One of most diffuse techniques for zeta potential investigation used in microfluidic science is the so-called current monitoring, first introduced by [20]. Initially, the channel is filled with a concentration solution c_1 and conductivity σ_1 and a voltage V_{ext} is applied across the two reservoirs. At the instant t_1 the higher potential reservoir is emptied out and filled with a the same buffer with higher concentration c_2 and conductivity σ_2. Due to the advection, the bulk fluid moves and the new

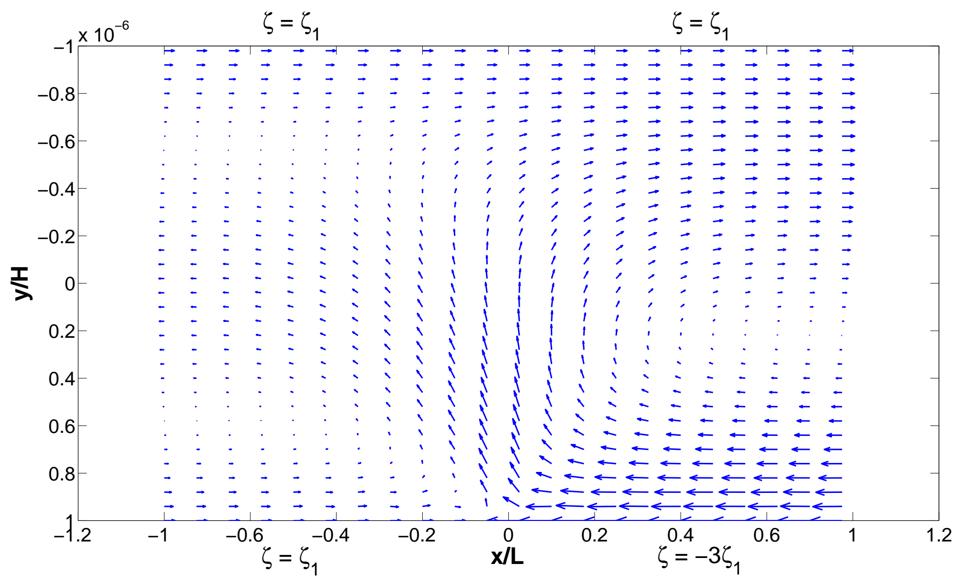

Figure 5.4: Velocity field with $\zeta_2 = -3\zeta_1$.

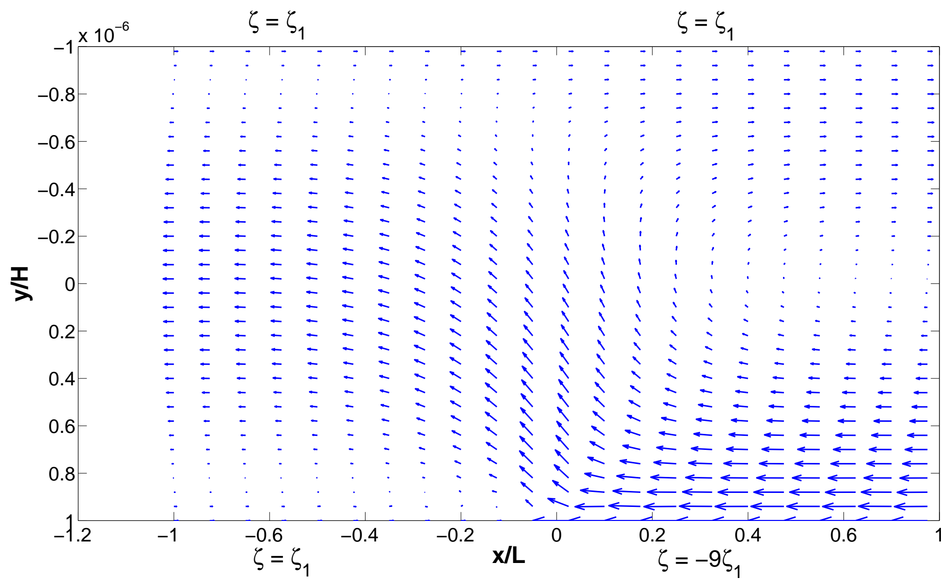

Figure 5.5: Velocity field with $\zeta_2 = -9\zeta_1$.

electrolyte substituted the older one increasing the conductivity of the channel. The total current, which is approximately the electromigration current, increases until the new steady state is reached at the instant t_2. Since the channel length is known, the velocity of the fluid can be calculated as

$$v_{\mathrm{EOF}} = \frac{L}{t_2 - t_1} \tag{5.1}$$

and the *zeta* potential of the channel can be derived from the Equation 3.1

$$\zeta = \frac{L}{V_{\mathrm{ext}}} \frac{\mu}{\epsilon_0 \epsilon_{\mathrm{b}}} v_{\mathrm{EOF}}. \tag{5.2}$$

The setup for current monitoring is shown in Figure 5.6. The keintler 2410 is used to apply voltage across the drain and the source and to measure the current through the channel. Keintler 6517 is used to measure the leakage current through the gate when a control voltage is applied using a voltage source.

Using a buffer with pH=4, low drain/source voltage has to apply to avoid bubbles formation. During the experiments was applied 10V, using platinum wire as electrodes to contact the buffer. This technique is usable to derive the zeta potential in a uniform channel or with low discontinuity. In our case, with the current monitoring is possible to obtain only an equivalent zeta potential, *i.e.* the one that will be with the channel will be uniform. From the current monitoring is possible to see the effect of the gate voltage on the curve shape. Using the numerical model, simulations of current monitoring are shown in Figure 5.8: higher is the concentration difference, greater is the difference from the equivalent ζ potential behavior. In Figure 5.7, the current monitoring profiles for the effective ζ potential, the numerical model and the actual data for a gate voltage of 200V are plotted.

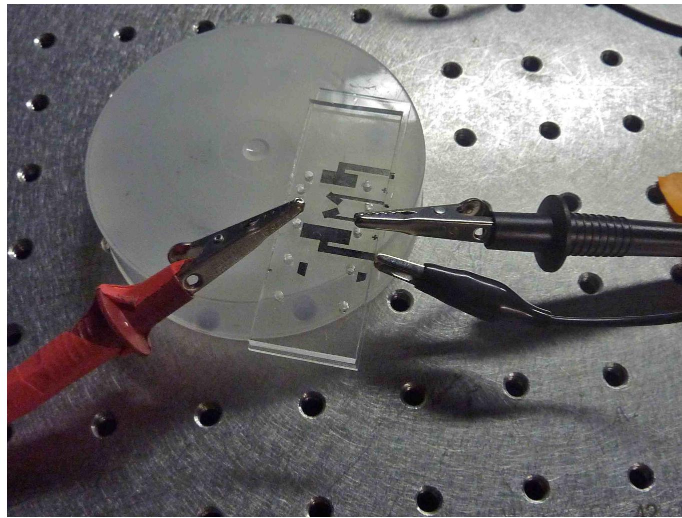

(a)

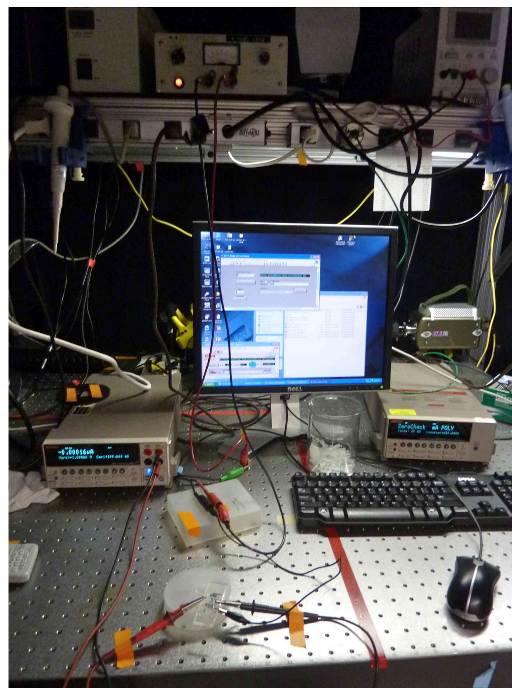

(b)

Figure 5.6: Particulars of the current monitoring setup.

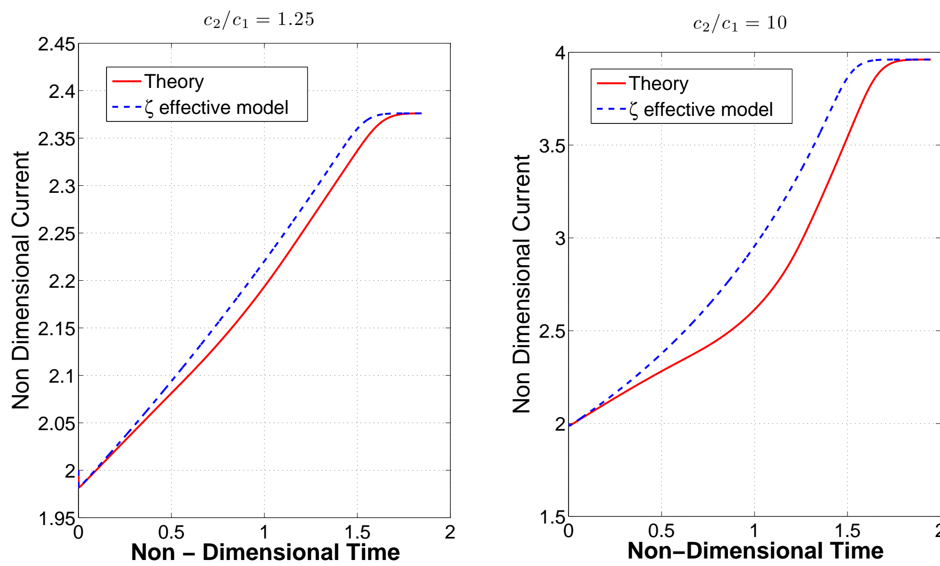

Figure 5.7: Simulation of the current monitoring.

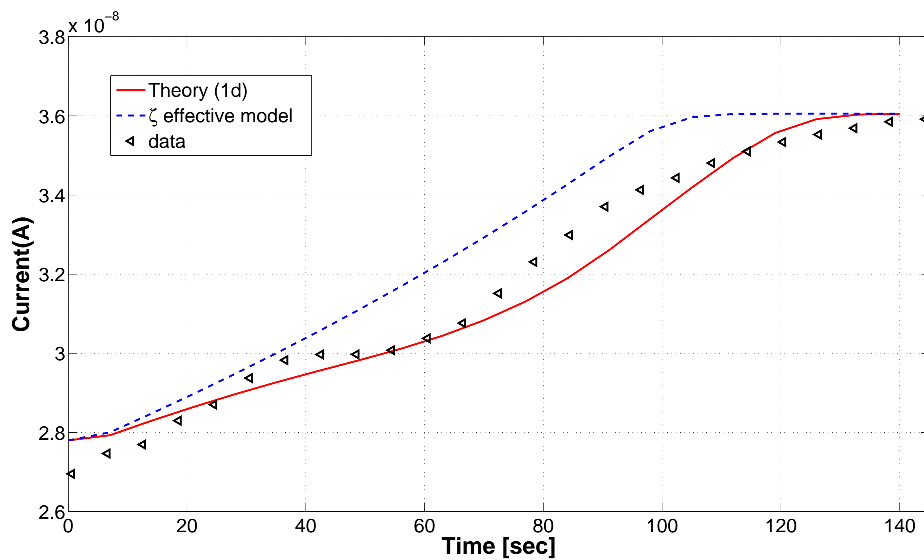

Figure 5.8: Comparison between simulated and measured current monitoring.

Chapter 6

Conclusion and Outlook

In the first part of the thesis we discussed the basic electrokinetic theory for developed a model for the Field Effect in microchannels. In particular, an equivalent electrical model was prepared to considered all the parameters that can influence the effects of a gate voltage applied in a device with a metal electrode insulated from the fluid. The circuit was analyzed with Matlab simulation to confirm the FET behavior. Then we moved to the fabrication process that involved several cleanroom steps to obtained a working device. An intensive work was done to product functional molds for PDMS microchannel. Finally the devices were tested with the current monitoring technique to confirm both the electrical model previous introduced and a numerical model that simulated the field velocity and the current monitoring profile inside the channel.

From the results obtained in the experimental section, a complicated flow takes place in the microchannel and the models make difficult to fit it. Further investigations will be performed in order to create a more accurate model. More in depth, also a feedback control will be studied and some coating techniques will be tested to make suitable the application of the field effect flow control to higher pH for biological applications.

Bibliography

[1] Nolan A. Polson and Mark A. Hayes. Electroosmotic flow control of fluids on a capillary electrophoresis microdevice using an applied external voltage. *Analytical Chemistry*, 72(5):1088–1092, 2000.

[2] Staffan Wall. The history of electrokinetic phenomena. *Current Opinion in Colloid & Interface Science*, 15(3):119 – 124, 2010.

[3] T. W. Healy D. E. Yates, S. H. Levine. Site-binding model of the electrical double layer at the oxide/water interface. *J. Chem. Soc., Faraday Trans. 1*, 70:1807–1818, 1974.

[4] L. R. White D. Chan, J. W. Perram and T.W. Healy. Regulation of surface potential at amphoteric surfaces during particle-particle interaction. *J. Chem. Soc., Faraday Trans. 1*, 71(3):1046–1057, 1975.

[5] N. J. Barrow A. M. Posner J. W. Bowden, S. Nagarajah and J. P. Quirk. Describing the adsorption of phosphate, citrate and selenite on a variable-charge mineral surface. *Australian Journal of Soil Research*, 18(1):49–60, 1980.

[6] A.M. Posner J. W. Bowden and J.P. Quirk. Adsorption and charging phenomena in variable charge soils. *Soils with variable charge, New Zealand Soc Soil Sci, DSIR, Lower Hutt, New Zealand*, pages 147–166, 1980.

[7] Luc Bousse, Nico F. De Rooij, and P. Bergveld. The influence of counter-ion adsorption on the [psi]0/ph characteristics of insulator surfaces. *Surface Science*, 135(1-3):479 – 496, 1983.

[8] K. L. Jensen and J. T. Kristensen. Theory of electrokinetic effects in nanofluidic channels. Bachelor thesis, Department of Micro- and Nanotechnology Technical University of Denmark, 2010.

[9] W Sparreboom, A van den Berg, and J C T Eijkel. Transport in nanofluidic systems: a review of theory and applications. *New Journal of Physics*, 12(1):015004, 2010.

[10] Alexandre Persat, Robert D. Chambers, and Juan G. Santiago. Basic principles of electrolyte chemistry for microfluidic electrokinetics. part i: Acid-base equilibria and ph buffers. *Lab on a Chip*, 9(17):2437–2453, 2009.

[11] Alexandre Persat, Matthew E. Suss, and Juan G. Santiago. Basic principles of electrolyte chemistry for microfluidic electrokinetics. part ii: Coupling between ion mobility, electrolysis, and acid-base equilibria. *Lab on a Chip*, 9(17):2454–2469, 2009.

[12] R. E. G. van Hal, J. C. T. Eijkel, and P. Bergveld. A novel description of isfet sensitivity with the buffer capacity and double-layer capacitance as key parameters. *Sensors and Actuators B: Chemical*, 24(1-3):201 – 205, 1995.

[13] Roberto Venditti, Xiangchun Xuan, and Dongqing Li. Experimental characterization of the temperature dependence of zeta potential and its effect on electroosmotic flow velocity in microchannels. *Microfluidics and Nanofluidics*, 2:493–499, 2006. 10.1007/s10404-006-0100-0.

[14] B. J. Kirby and E. F. Hasselbrink. Zeta potential of microfluidic substrates: 1. theory, experimental techniques, and effects on separations. *Electrophoresis*, 24(2):187–202, 2004.

[15] B. J. Kirby and E. F. Hasselbrink. Zeta potential of microfluidic substrates: 2. data for polymers. *Electrophoresis*, 24(2):203–213, 2004.

[16] B. E. Deal and A. S. Grove. General relationship for the thermal oxidation of silicon. *Journal of Applied Physics*, 36(12):3770–3778, 1965.

[17] Koh etch rate of silicon. `http://cleanroom.byu.edu/KOH.phtml`.

[18] H. Seidel, L. Csepregi, A. Heuberger, and H. Baumgärtel. Anisotropic etching of crystalline silicon in alkaline solutions. *Journal of The Electrochemical Society*, 137(11):3612–3626, 1990.

[19] A. Y. N. Sofia and C. Martin. A vapor-assisted method for adhering polydimethylsiloxane and glass. *Lab on a Chip*, 10:250–253, 2010.

[20] Xiaohua Huang, Manuel J. Gordon, and Richard N. Zare. Current-monitoring method for measuring the electroosmotic flow rate in capillary zone electrophoresis. *Analytical Chemistry*, 60(17):1837–1838, 1988.